Identifying Space-Resolved Proteins of the Murine Thymus, by Combining MALDI Mass Spectrometry Imaging and Proteomics

Jennifer T. Aguilan[1,2], Carlos Madrid-Aliste[2,3], Maria K. Lagou[4], Simone Sidoli[2,5,†], George S. Karagiannis[4,6,7,8,9,10,†]

[1]Department of Pathology, Albert Einstein College of Medicine, Bronx, NY, USA
[2]Laboratory for Macromolecular and Proteomics Facility, Albert Einstein College of Medicine, Bronx, NY, USA
[3]Department of Systems and Computational Biology, Albert Einstein College of Medicine, Bronx, NY, USA
[4]Department of Microbiology & Immunology, Albert Einstein College of Medicine, Bronx, NY, USA
[5]Department of Biochemistry, Albert Einstein College of Medicine, Bronx, NY, USA
[6]Gruss-Lipper Biophotonics Center, Albert Einstein College of Medicine, Bronx, NY, USA
[7]Tumor Microenvironment Program, Montefiore-Einstein Comprehensive Cancer Center, Bronx, NY, USA
[8]Integrated Imaging Program for Cancer Research, Montefiore-Einstein Comprehensive Cancer Center, Bronx, NY, USA
[9]Cancer Dormancy Institute, Montefiore-Einstein Comprehensive Cancer Center, Bronx, NY, USA
[10]Marilyn and Stanely M. Katz Institute for Immunotherapy for Cancer and Inflammatory Disorders, Montefiore-Einstein Comprehensive Cancer Center, Bronx, NY, USA

[†]Indicates co-corresponding authorship

ABSTRACT

The identification of spatially resolved proteomes has recently seen significant breakthroughs, yet challenges persist, particularly in integrating protein identification with precise spatial localization within a single experimental workflow. Matrix-assisted laser desorption ionization mass spectrometry imaging (MALDI-MSI) enables spatial protein mapping on tissue sections without the need for antibodies. While MALDI-MSI addresses several obstacles in proteomic mapping with spatial resolution, it remains limited in its capacity for definitive protein identification. To overcome these limitations, this study introduces a novel approach combining MALDI-MSI with liquid chromatography-mass spectrometry (LC-MS/MS) to map protein localization and spatial changes in thymic tissue. Using a mouse model of chemotherapy-induced thymic involution with time-dependent regeneration kinetics, we evaluated the capability of this pipeline to resolve proteomic changes in a spatiotemporal manner. Our approach incorporates a scoring system to align molecular signals from MALDI-MSI with proteomic data, enabling precise identification of proteins critical for thymic function. The results reveal key changes in protein expression, particularly in regions associated with cell migration, cytoskeletal remodeling, and endogenous thymic regeneration. By analyzing the spatial distribution of proteins such as Keratin 8 (KRT8), Nucleoporin TPR, Cysteine- and Glycine-Rich Protein 3 (CSPR3), and Tubulin-Associated Chaperone-A (TBCA), we observed distinct shifts in thymic compartment architecture, underscoring the impact of chemotherapy on thymic tissue structure. From a translational viewpoint, this approach identifies new pathways and targetable candidates to enhance immune cell recovery in pediatric cancer patients undergoing cytoreductive treatments. From an analytical perspective, it provides an innovative framework for visualizing protein distribution in lymphoid and other tissues, significantly advancing the potential for translational proteomic research.

Keywords: imaging, mass spectrometry, thymus, chemotherapy

INTRODUCTION

The identification of spatially resolved proteomes has been a challenge that only recently met some breakthroughs[1]. While advanced instrumentation and time-consuming protocols can identify proteomes to resolve single-cell identity and heterogeneity, imaging mass spectrometry experiments are still limited due to limitations in combining protein identification with respective localization in a single experimental run. Matrix assisted laser desorption ionization - mass spectrometry imaging (MALDI-MSI) is a technique that circumvents such issues. MALDI-MSI is capable of performing spatial mapping of peptides or proteins directly on either a flash frozen or FFPE tissue section. One main advantage of MALDI-MSI over traditional immunohistochemistry is that it does not require antigen-specific antibodies to map locations of peptides or proteins on the tissue. Therefore, it is a very useful molecular histology tool for both screening and multiple detection of potential new biomarkers for diseases. However, MALDI-MSI is generally limited due to the low signal-to-noise ratio[2] and the limited capability of performing MS/MS fragmentation of candidates, which reduces the specificity of detection[3]. In this work, we used MALDI-MSI as an unbiased approach for resolving organ/tissue compartmentalization by studying differential expression of proteins through on-tissue peptide spatial mapping. To serve these needs, we adopted an established mouse model of acute thymic involution[4], an organ pathology for which MALDI-MSI has not been previously used to extrapolate biological insights.

The thymus is a primary lymphoid organ of T cell development and maturation and sits encapsulated above the heart in the mediastinum. The thymus consists of two lobes that divide into lobules, which in turn, are subdivided into two distinct zones, an outer cortex and an inner medulla. These compartments embody functional “niches” that provide essential spatiotemporal signals that regulate key processes of T cell development, in particular thymocyte homing, survival and expansion, as well as T cell receptor chain rearrangement, and the establishment of central tolerance. In both embryonic and non-embryonic thymuses, these processes are spatially orchestrated by an intrathymic stromal network of cortical (cTEC) and medullary (mTEC) thymic epithelial cells, as well as by a supporting network of non-epithelial stromal cells, such as fibroblasts, blood vessel endothelial cells and their associated pericytes, etc. All these stromal cells, either epithelial or non-epithelial, reside in and specialize their functions in distinct cortical and medullary thymic compartments[5-20].

During preadolescence, the thymus plays an essential role in establishing a comprehensive and enduring T cell repertoire, which is pivotal for systemic immunity, immune surveillance, and the establishment of central tolerance[21-23]. Notably, this period marks the zenith of the thymus’s functional capacity, which subsequently experiences a progressive, age-related decline. By ear-

ly adulthood, the reliance of systemic immunity on the thymus decreases, shifting towards increased dependence on the expansion of peripheral memory T cells[24-29]. More importantly, the thymus is particularly vulnerable to a variety of cytotoxic agents, leading to its rapid (acute) thymic involution (ATI)[30-35]. For instance, treatment of cancer patients with cytoreductive chemotherapy leads to both short- and long-term consequences on systemic immunity, mainly due to ATI[30,31,35-37]. Given the key role of the thymus in immune development in children, ATI emerges as pressing concern for pediatric cancer patients undergoing cytoreductive treatments, thus necessitating meticulous consideration to alleviate its effects on systemic immunity. Administration of chemotherapy and radiotherapy exacerbates ATI and compromises the immune system, thus making pediatric patients vulnerable to infections, and challenging the recovery of the immune system post-therapy[30,35]. Strategies aimed at fostering endogenous thymic regeneration during or subsequent to chemo/radiotherapy hold the promise of significantly improving life expectancy and quality-of-life for pediatric cancer survivors. However, progress in understanding thymic function and recovery post-cytotoxic treatment has been limited, especially due to the lack of systemic approaches like single-cell transcriptomics and high-throughput proteomics. Advancing these techniques in this field could significantly enhance our ability to restore immune functions and competence in pediatric cancer patients.

In addition, given the histological perplexities of lymphoid organs, including the thymus as described above, it would be imperative to implement spatial resolution in such sophisticated analytical techniques, to be able to gain sufficient and valuable information for complicated processes, such as endogenous regeneration following chemotherapeutic insult. Since MALDI-MSI circumvents these caveats by generating a large set of imaging spectra, here, we adopted a method for unsupervised hierarchical clustering of similar spectra to extract principal components, i.e. signals that univocally characterize regions of interest within thymic tissues. Upon compiling a library of candidates, we then utilized LC-MS/MS analysis of serial or adjacent thymic tissue sections, to create a list of candidate peptides detectable in the samples. We subsequently engineered a peak-matching pipeline with a customizable scoring system, to match LC-MS/MS with MALDI-MSI data, and prioritize candidates based on identification confidence and quantification. In summary, this newly proposed methodology applies the techniques of MALDI-MSI and LC-MS/MS in parallel tissue slide sections, to identify potential protein markers of thymic compartmentalization and endogenous thymic regeneration, in a mouse model of chemotherapy-induced involution. Compared to more routine proteomics experiments, our pipeline combines in a single shot the identification of potential candidate biomarkers with feasibility assays, to assess the capability of MALDI-MSI in confidently quantifying these signals.

METHODS

Mouse Model of Cyclophosphamide-Induced Thymic Involution. Cyclophosphamide monohydrate (Thermo Scientific) was reconstituted at a concentration of 25 mg/mL in sterile Phosphate-Buffered-Saline (PBS). Each mouse in the experimental group received an *i.p.* dose of 200 mg/Kg of Cyclophosphamide monohydrate in sterile PBS (200 µL total volume), every 3 days, for a total of 3 doses. The control (vehicle-treated) mouse group received an *i.p.* injection of 200 µL sterile PBS. The last day of chemotherapy treatment was designated as "Day 0". The mice were then blindly categorized into five subgroups. Mice from either control or experimental subgroups were sacrificed on a weekly basis for up to 5 weeks post-chemotherapy i.e., Day 35. Mouse thymi were dissected using standardized autopsy procedures, and were cleaned from peri-thymic adipose tissue, carefully without damaging the thymus. Experiments were replicated in at least three independent mouse cohorts (N=5 mice per group).

MALDI-MSI Analysis of Mouse Thymus Tissue Sections (Fig. 1A). FFPE thymic tissue sections, cut at 5 µm thickness, were mounted on indium-tin oxide (ITO) conductive glass slides. The FFPE tissue sections were deparaffinized for 1.5 h at 60-65 ^{o}C and washed through a series of xylene, 100%, 95%, 70% ethanol and water. Tissue slides in 10 mM Tris buffer were heated to 95-98 ^{o}C using a steamer for 30 min. Slides were cooled down, buffer exchanged with water and dried in desiccator overnight. The tissue slides were then spray-coated with trypsin solution using the TM Sprayer (HTX Technologies). The slides were air dried for 5 min and then incubated in a hydrated chamber for overnight trypsin digestion at 37 ^{o}C. After digestion, slides were dried for 15 min in the vacuum desiccator and then spray coated with CHCA matrix (α-cyano-hydroxycinnamic acid; 5 mg/ml in 50% AcN/0.2% TFA) using the TM Sprayer (HTX technologies). Peptide spatial mapping was performed by scanning and acquiring spectra m/z range 700-3,500) at 100 µm raster width using the UltrafleXtreme MALDI TOF/TOF mass spectrometer (Bruker Daltonics) (Figure 1). After the MALDI imaging analysis, the matrix was washed off from the tissue and followed by staining with Hematoxylin and Eosin (H&E).

Spectra are processed by pre-defined smoothing and baseline subtraction. To remove variations in pixel-to-pixel intensities, TIC (mean) normalization was performed by dividing all spectra by the means of all data points. Using Fleximaging v 4.0, unsupervised hierarchical clustering based on Euclidean distance metric and Ward linkage was performed to generate segmentation maps from the images acquired from the tissue samples. The dendrogram was generated with only the top nodes displayed. To go deeper into the dendogram, the "+" sign is selected to ex-

pand the tree. The numbers in brackets are the number of mass spectra belonging to the same node while the number before it can be the node ID or the cluster distance. The selected branch generates a display filter assigned to a specific color for clustering pixels with similar spectra. This generates a spatial heat map that use a color intensity scale to show the varying intensity ratios of mass signals observed from different areas on the tissue.

LC-MS/MS and protein identification (Fig. 1B). Serial or adjacent FFPE tissue sections at 5 µm thickness were mounted on positively charged regular microscope glass slides. The FFPE tissue sections were deparaffinized for 1.5 h at 60-65 ^{o}C and washed through a series of xylene, 100%, 95%, 70% ethanol and water. Tissue slides in 10 mM Tris buffer were heated to 95-98 oC using a steamer for 30 min. Slides were cooled down, buffer exchanged with water and dried in desiccator overnight.[53] The tissue slides were then spray coated with trypsin solution using the TM Sprayer (HTX Technologies). The slides were air dried for 5 min and then incubated in a hydrated chamber for overnight trypsin digestion at 37 ^{o}C. After digestion, slides were dried for 15 min in the vacuum desiccator. The peptides were sequentially extracted twice each by pipetting 30 ul of 0.1% triflouroacetic acid and 60% acetonitrile/ 0.1 triflouroacetic acid, collected and pooled into Eppendorf microcentrifuge tube.

The peptide digests were desalted using C-18 ziptip or Oasis HLB resin by vacuum filtration and eluted with 60% acetonitrile/0.1% TFA, concentrated in a speed vacuum and re-suspended in 0.1% acetonitrile and analyzed by LC-MS/MS using a nanoRSLC U3000 (Dionex, Thermo Scientific) or a nanoAcquity UPLC (Waters) connected to Orbitrap Exploris 480 (Thermo Scientific). The LC gradient composed of 120 minutes for 4% - 34% solvent B (Solvent A: 0.1% Formic acid and Solvent B: 80% Acetonitrile/0.1% Formic acid).

For peptide identification and label free quantification, the MS/MS data obtained from DDA were searched by the SEQUEST search engine using Proteome Discoverer v2.5 (Thermo Scientific). Protein abundances were log2 transformed and normalized and statistical differences between protein relative abundances were assessed using a t-test as previously discussed. Automated database search was performed by Proteome Discoverer v2.5 using Sequest search engine. MS/MS data obtained from DDA searched against SwissProt mouse database with the following parameters: missed cleavage = 2; carbamidomethylation on C; oxidation on M; deamidation on N and Q; peptide tolerance = 10 ppm; MS/MS tolerance = 0.02 Da for MS/MS spectra acquired in the orbitrap analyzer.

PepBridge: The MALDI-MSI and LC-MS/MS peak matching pipeline. The MALDI imaging data from the average spectrum was first processed by reducing the bin size to 4,000 and then converted to a .csv file containing m/z vs MALDI average intensities. The .csv file is converted to an Excel file and the exported peptide table obtained from the LC-MS/MS analysis was pasted into the same file. The peptide table was sorted by the highest intensity of MALDI peaks and further processed by an in-house developed program (pepBridge.py) described in detail in **Supplementary Materials & Methods** and **Fig. S3**, and can be downloaded from this link: https://github.com/carlos-madrid-aliste/pepBridge.The m/z with a filter of +/- 0.5 or +/- 1.0 Da was used in order to match the MALDI m/z with the corresponding theoretical $[M+H]^+$ for each peptide identified from the LC-MS/MS analysis. MALDI-LC/MS/MS matches that have MALDI average intensities below the arbitrarily assigned noise cut-off filter of 2.0 were filtered out. Both MALDI average intensities and LC-MS/MS intensities were *log2* transformed. Each *log2* transformed peptides was normalized by the average intensities of the all the peptides identified per sample. Because MALDI-TOF suffers from low resolution and peak widths are broader compared to narrower peaks obtained from high resolution mass spectrometers used for LC-MS/MS such as the orbitrap, Hence, a single peptide peak observed from MALDI-TOF with corresponding peptide ion heat map can potentially match to ≥1 peptide candidate observed from LC-MS/MS. To provide a basis for ranking of top peptide candidates based on probabilities, we developed a MALDI-LC-MS/MS peak matching pipeline which served as a (prioritization) scoring system, based on four (4) metrics:

Metric 1: Delta of log2 ratios or log2 fold changes between MALDI and LC-MS/MS. The differences between the *log*2 fold changes of “Chemo treated” vs “Control” between MALDI and LC-MS/MS were calculated and sorted from lowest to highest and plotted against the scores. The highest score, y = 10 corresponds to smallest delta or difference between the *log2* fold changes of “Chemo treated” vs “Control” obtained from MALDI and LC-MS/MS. Hence, a Gaussian curve is generated with the x centered at 0 *log2* fold change versus the y maximum of 10. The formula is $f(x) = A \cdot e^{-[(x-\mu)^2/2\sigma^2]}$ where x is the input variable, A is the amplitude, which is the maximum value of the distribution, μ is the mean (or the center) of the distribution and σ is the standard deviation that controls the spread of distribution. Since A is assigned to be the highest score of 10 and the x = 0 to be at the center, the formula now becomes $f(x)=10 \cdot e^{-[(x)^2/2\sigma^2]}$. This is converted to an Excel formula, y = 10*EXP(-A1^2/(2*(B1^2))) where A1 represents the cell containing the input value of x (delta log2 fold change), and B1 represents the standard deviation derived from all the delta *log2* fold changes. This formula calculates the y values based on a Gaussian distribution using the specified parameters.

Metric 2: Delta mass between MALDI and LC-MS/MS. The differences between the peptide masses observed from MALDI and LC-MS/MS were calculated. The highest score of y = 100 corresponds to the x with the smallest difference as x approaches 0 while the minimum score of y = 0 corresponds to x with the biggest peptide mass difference observed from MALDI and LC-MS/MS as x approaches 1. The function would be $f(x)=1/1+e^{k(x-x0)}$ where x is the computed delta mass, x0 is the central value where x = 0.5 and k is the steepness parameter. In Excel, the formula is y = 100/(1+EXP(10*(A1-0.5))) where A1 is the computed delta mass, the steepness parameter, k = 10 and central value x = 0.5. This formula calculates the y values based on the negative sigmoid function with the central value x = 0.5.

Metric 3: MALDI intensity. The third metric is the MALDI intensities. The higher the intensity means the higher score where y = 5 as the maximum score while y = 0 is the minimum score versus x which are the MALDI intensities with a central value of x = 2. So, the function is, $f(x)= 5/1+e -k^{(x-2)}$, where y = 5 is the maximum score, k is the steepness parameter, and x is the MALDI intensity. In Excel, the formula is, y = 5/(1+EXP(-A1+2)), where A1 is the input value, which is the MALDI intensity and the steepness parameter, k = 1. This formula calculates the y values based on the sigmoid function using the specified parameters.

Metric 4: Matching with the image or the peptide ion heat map. The scores from Metrics 1 to 3 are summed, with the highest total representing the top candidate peptide, followed by the other candidate peptides corresponding to a specific MALDI peak (m/z). Metric 4 serves as the final criterion, aligning the peptide's spatial mapping or MALDI molecular image with both the log-fold changes and peptide scores.

Bioinformatic characterization of prioritized candidates. The protein accession numbers of the prioritized candidate proteins (N=68) were submitted to STRING v12.0[38], for functional network association analysis. The network was visualized by confidence meaning of network at medium confidence (0.4), and all active interaction resources were included in the analysis. The k-means clustering approach was selected for classifying the protein subnetworks into thematic clusters involving distinct biological/molecular concepts.

Immunofluorescence. Thymi from vehicle- and cyclophosphamide (CTX)-treated FVB/NCrl mice were fixed in 10% Neutral Buffered Formalin for 48h, processed and paraffin embedded. 5um sections were deparaffinized and dehydrated in double changes of xylene and 100, 95, 70 degrees alcohol, respectively, followed by rehydration. Citrate (Novus Biologicals, Cat. No. NB90062075) and EDTA (Epredia, Cat.No. AP9004500) antigen retrieval was performed with a steamer for 21minutes. The blocking step was performed with 5% goat serum (R&D systems,

Cat.No. S13110) in 0.05% PBS-Tween20 for one hour, after which the slides were incubated with the following primary antibodies overnight at 4°C:, TBCA (Rabbit, polyclonal, Invitrogen, Cat.No. PA5-51186), CSRP3 (Rabbit, polyclonal, Invitrogen, Cat.No. PA5-109602), TPR (Rabbit, polyclonal, Invitrogen, Cat.No.PA5-95533), KRT5 (Chicken IgY, purified polyclonal, Biologend, Cat.No. 905904), KRT8 (Guinea Pig, polyclonal, Origene, Cat.No BP5075). All antibodies were used at 1:100, except KRT5, which was used at 1:300. The secondary antibody incubation was performed with the following antibodies at 1:200 dilution for 50 minutes: goat anti-Rabbit Alexa Fluor488 (Invitrogen, Cat.No. A11034), goat anti-Chicken IgY Alexa Fluor488 (Invitrogen, Cat.No. A11039), goat anti-Guinea Pig Alexa Fluor555 (Invitrogen, Cat.No. A21435), followed by nuclear staining for 5 minutes with DAPI (4,6-Diamidino-2-phenylindole dihydrochloride, Novus Biologicals, Cat.No NBP231156) and mounting with ProLong Gold antifade mounting reagent (Invitrogen, Cat.No. P36934).

Slides were left to dry overnight at dark, and subjected for digital scanning via a 3D HISTECH P250 Flash III automated slide scanner, using a 20x 0.75NA objective lens into a multichannel overlay image, as described in prior work from our group[39-42]. All the slides used were subjected to the same color adjustment for each marker in CaseViewer version2.4 software.

Histopathology. Hematoxylin and eosin (H&E) staining was conducted with the same deparaffinization procedure as described above; upon which Hematoxylin incubation for 5min, differentiation for 5sec, Eosin Y stain for 1min45sec followed, before clearing in 95,100 degrees alcohol, and xylene and mounting with Permount (SP15-100, Fisher).

RESULTS

Pipeline Overview. A graphical summary of the pipeline followed in this work is presented in **Figure 1**. Briefly, FFPE tissue sections are prepared for protein digestion using a TM sprayer, and analyzed by MALDI-MSI **(Fig. 1A)**. In parallel, digested peptides from the thymic tissues are collected, dried, and analyzed by LC-MS/MS **(Fig. 1B)**. An integration of these parallel datasets, via our newly-developed, customizable, highly-versatile algorithm PepBridge **(Suppl. Methods)**, leads to candidate markers of thymic compartmentalization and endogenous regeneration after chemotherapy treatment.

Mouse model of cyclophosphamide-induced thymic involution. We used digital pathology to examine whole slides of murine thymi **(Fig. 2A)**. Under normal conditions, the murine thymus is surrounded by a connective tissue capsule **(Figs. 2A-C)**, which is composed of fibroblasts, blood vessels, and collagen fibers[43-46]. The capsule invaginates to the organ's interior, forming connective tissue trabeculae, also known as "septae" **(Figs. 2A-D)**, which correspond to the routes of inbound and outbound blood vessels and nerves[43-46]. These septae segregate the thymus into basic structural/functional units, thymic lobules **(Fig. 2B)**[43-46]. There are two distinct zones identified within the thymic lobules, an "outer" darker zone, which is characterized by small lymphocytes and is called "cortex", and an "inner" lighter zone, which is mainly comprised by larger lymphocytes and is called "medulla"[43-46] **(Figs. 2A-D)**. Functionally, the cortex determines total thymopoietic capacity, while the medulla orchestrates the negative selection, thus establishing central tolerance. Interestingly, thymic compartmentalization via the connective tissue septae is not complete, as the septae never physically interact with one other in the medullary regions. As such, the thymic medulla is often visualized as a single and relatively continuous entity **(Fig. 2A)**, depending on the orientation of the tissue section[43-46]. A microanatomical region of great functional importance is the corticomedullary junction (CMJ), represented as a tentative border between cortex and medulla **(Fig. 2E)**, in which the trabecular vessels branch out, creating the CMJ vessels **(Fig. 2E)**[43-46]. These vessels are opted for the immigration of early thymocyte progenitors (ETPs) in the thymus, as well as for the egress of mature $CD4^+$ or $CD8^+$ T cells in the peripheral blood[43-46].

Acute thymic involution in mice occurs after the administration of cytotoxic agents such as chemotherapy, corticosteroids, antibiotics, and other drugs, and physiologically mimics human responses[30,31,34,35]. Cyclophosphamide, an alkylating agent that is often administered in the course of chemotherapy treatment in cancer patients, is a well-established immunosuppressive

drug with deliberating consequences on the thymus[37,47-51]. To monitor global proteomic changes during endogenous thymic regeneration after chemotherapy, here, we developed a mouse model of cyclophosphamide-induced thymic involution by exposing female FVB mice into radical doses of cyclophosphamide (i.e., 200mg/Kg every 3 days), followed by five weeks of monitoring post-chemotherapy. This experimental pipeline allowed us to capture precise kinetics of endogenous thymic regeneration following the chemotherapeutic insult **(Fig. 2F)**, a process often deemed complex due to the plethora of signaling circuitries regulating thymic remodeling[36,52,53]. We noted marked thymic involution on the first week following chemotherapeutic insult, characterized by ambiguous corticomedullary junction and hypoplastic cortex **(Fig. 2G)**. Endogenous thymic regeneration was relatively fast, with the thymic mass reaching an equilibrium by the second week following the chemotherapeutic insult **(Fig. 2G)**. Interestingly, there was a relative increase of thymic size by the third and fourth weeks of endogenous thymic regeneration **(Fig. 2G)**, which is consistent with prior observations of "rebound hyperplasia" in human patients receiving chemotherapy[54-62]. Rebound hyperplasia, whose peak was at 3rd week following chemotherapeutic insult (**Fig. 2G)**, was characterized by excessive cortical hyperplasia and a disanalogous medullary compartment, resulting in evident increase of the corticomedullary ratio **(Fig. 2H)**. A "recoil" phase between 4th-5th week following the chemotherapeutic insult, during which thymic size reverted back to its homeostatic/equilibrium size, was captured as the final step of endogenous thymic regeneration **(Fig. 2G)**. Overall, the impact of cyclophosphamide on the murine thymus and the associated kinetics **(Fig. 2G)** are consistent with prior reports[4,37,50,63,64].

Hierarchical clustering of MALDI-MSI acquired spectra from the murine thymus. To identify biomarkers predictive of thymic regeneration, we leveraged the detailed kinetics of endogenous thymic renewal following cyclophosphamide (Ctx)-induced injury. We focused on the 21-day post-Ctx timepoint for several reasons. First, although "rebound hyperplasia" is commonly observed in patients after chemotherapy or other anticancer treatments, no established biomarkers currently gauge thymic functionality during this condition. Second, to our knowledge, a spatially resolved proteome map has never been generated for regenerating thymus, particularly during rebound hyperplasia.

With these considerations, we collected thymi from vehicle-treated and Ctx-treated mice 21 days after ending their respective treatments **(Fig. 2F)**. The tissues were processed as FFPE samples and subjected to MALDI-MSI following our established pipeline **(Fig. 1A)**. From this analysis, we obtained comprehensive mass-to-charge (m/z) maps, which were processed using

Fleximaging v4.1 to extract signals uniquely defining specific regions-of-interest. To correlate these molecular patterns with anatomical features, the same thymic sections used for MALDI-MSI were also stained with H&E. This enabled the direct superimposition of molecular images onto histological structures.

We then performed unsupervised hierarchical clustering of the spectra to identify unique features represented by distinct nodes in the resulting dendrogram **(Fig. S1)**. This approach generated segmentation maps from the acquired tissue images, assigning specific colors to groups of pixels that shared similar spectral signatures. We then extracted three highly unique m/z values that defined each cluster, specifically those at 946 Da, 1337 Da and 1454 Da, and generated their corresponding extracted ion images. Interestingly, each of these three signals—946 Da, 1337 Da, and 1454 Da—represented a different cluster and compartment of the thymus **(Fig. S2)**. Assigning a distinct color to each signal generated individual ion heat maps, which, when overlaid, demonstrated that the spatial relationships among the three signals were preserved. Reconstructing molecular images from the 946 Da, 1337 Da, and 1454 Da signals revealed compartment-specific expression patterns within the thymus **(Figs. 3A–D)**. For example, the 1454 Da signal delineated the thymic capsule, various stromal elements, and surrounding connective tissues **(Fig. 3B)**. The 946 Da signal marked elements expressed predominantly in the medulla, though also present in the cortex **(Fig. 3C)**. In contrast, the 1337 Da signal was expressed throughout the thymus, with a stronger presence in the cortex **(Fig. 3D)**.

Interestingly, some molecular images also revealed differences between normal thymus and thymus undergoing rebound hyperplasia following cyclophosphamide. The 946 Da signal, for instance, showed a clear corticomedullary distinction in vehicle-treated controls but presented a less defined pattern in the Ctx-treated thymus **(Fig. 3C)**. This suggests that the corresponding protein may be reduced or functionally altered during the endogenous regenerative process. In summary, our MALDI-MSI approach accurately mapped expected thymic compartmentalization, including peri-thymic connective tissue encapsulation and distinct corticomedullary zones, while also revealing histological changes in thymic architecture under experimental conditions. Our next step was to identify the major discriminating signals uncovered by these analyses.

LC-MS/MS proteomics analysis of peptides collected from tissue digestion. One challenge in MALDI-MSI is the assignment of precise identities to the obtained signals. To address this challenge, we performed proteomic analysis of extracted peptides from the tissue slides, which consisted of an online LC-MS/MS using data-dependent acquisition **(Fig. 1B)**. The analysis identified 6,489 and 6,538 peptides corresponding to 1,786 and 1,801 proteins from the Ctx-

and vehicle-treated conditions, respectively **(Fig. 4A)**. Identified peptides were label-free quantified, to determine the fold change enrichment between the treated and untreated conditions **(Fig. 4B)**. Notably, just a few proteins were found at very high abundance, while the majority of identifications were concentrated among less abundant signals **(Fig. 4C)**. With this analysis, we obtained a list of identifiable targets present in thymic tissues, which could be subsequently matched to the MALDI-MSI discriminant peaks.

MALDI-LC-MS/MS peak-matching pipeline (pepBridge) combined with a 4-metric scoring system. The major challenge in this step is the issue related to the relatively low resolution of MALDI-TOF mass spectrometry (40,000 at m/z 400) compared to the higher resolution provided by orbitrap mass spectrometry (120,000 at m/z 200) utilized in the LC-MS/MS experiment. With a mass tolerance for MALDI-MSI spectra set at ± 0.5 Da, it frequently happened that more than 1 peptide candidate identified in the LC-MS/MS runs matched with the potential m/z. For this reason, we developed PepBridge, a MALDI-LC-MS/MS peak matching pipeline based on four rationally-designed metrics based on: (1) delta fold change; (2) delta mass; (3) MALDI intensity and (4) matched image or ion heat map. Each peptide mass identified from LC-MS/MS and matched to MALDI receives a score from each of the metric. The sum of the peptide scores from the Metrics 1 to 3 were used to rank the probabilities of peptide match. The highest score corresponds to top peptide candidate with the highest matching probability and whose sequence belongs to a particular protein. As positive control, we utilized trypsin that was sprayed on the MALDI plate and selected regions of interests at specific locations outside the tissue sections that are expected to contain only trypsin (**Fig. S1 A, A', A" and Fig. S2 A, A'**). The PepBridge scoring system revealed that the tryptic peptides were the most enriched obtaining the highest score and most importantly, validated our scoring pipeline **(Fig. S4 and Table S1)**.

The imaging data obtained from the thymus control and treated tissue sections were further processed using the PepBridge MALDI-LC-MS/MS peak matching pipeline. A mass filter of +/- 1 Da was applied in order to include those broad peaks that potentially contain overlapping peptide peaks that could be missed if the mass filter is too narrow or stringent. There were about 23,000 MALDI-LC-MS/MS matches that were further filtered by setting a signal-to-noise cut-off filter of 2.0 such that all hits below this filter are removed **(Figs. 5A-B; Table S2)**. After the signal-to-noise filter, the list was narrowed down to 676 matches corresponding to 676 peptides. To facilitate the selection of the top peptide candidates, the peptides were scored based on metrics 1 to 3 **(Fig. 5C-E)**. The Peptide Score is the summed scores from Metrics 1 to 3 for each peptide **(Table S2)**. This corresponds to the rank of the peptide or its matching probability. In-

terestingly, we found that ranking the peptides within its protein group proved to be more effective in selecting the top peptide candidates by manually comparing the peptide scores and the log fold changes within a protein group. The fourth and final metric, i.e. the correspondence with a clustered signal when the MALDI-MSI image was extracted, was used to further screen the peptide candidates by comparing the image versus the log-fold changes. This step involved a combination of visual inspection and manual matching of the MALDI images with the metric scores **(Fig. S4)**. The list was further narrowed down to a final table of 68 candidates **(Table S2)**, which to our knowledge, represents the largest spatiotemporally characterized proteome during endogenous thymic regeneration following chemotherapy insult.

Protein-protein interaction (PPI) analysis reveals organized networks of thymic compartmentalization and endogenous thymic regeneration following cyclophosphamide insult. The 68 candidate proteins identified through PepBridge were subjected to protein-protein interaction (PPI) analysis using STRING, followed by k-means clustering, to infer physical and functional association networks **(Fig. 6)**. The analysis revealed that most of the proteins were interconnected, forming a total of four functional PPI networks. Eight proteins (Ubxn1, Tbca, Numa1, Kansl3, Cbr1, Vac14, Rab14, Marcksl1) did not associate with any network, while a small two-protein network, composed of only fibrinogen-alpha (Fga) and tissue factor (F3), stood apart from the larger interconnected clusters **(Fig. 6)**. The remaining three networks consisted of approximately 15 proteins each, loosely arranged and lacking strongly centralized hub proteins, with few exceptions, such as vimentin (Vim), 60S ribosomal protein L7 (Rpl7a), and heterogenous nuclear ribonucleoprotein M (Hnrnpm). Instead, only few proteins displayed "hub-like" activity, maintaining "open" interconnections with other proteins rather than forming tightly centralized hubs **(Fig. 6)**. This lack of strong hub proteins may indicate that endogenous thymic regeneration relies on multiple and promiscuous pathways, rather than a few dominant regulatory mechanisms, a premise that is consistent with the existing literature suggesting a complex and distributed network of signaling pathways underpinning endogenous thymic regeneration[31,34,65].

The first cluster identified, *Intermediate Filament Organization*, consists of structural proteins and regulators of cytoskeletal rearrangements, including Keratin 5 (Krt5), Keratin 7 (Krt7), Keratin 8 (Krt8), Vimentin (Vim), Marker of Proliferation Ki-67 (Mki67), Wiskott-Aldrich Syndrome Protein (Was), and Ras Homolog Family Member G (Rhog), among others **(Fig. 6)**. These proteins are critical for maintaining thymic architecture and supporting thymopoiesis. In principle, keratins and vimentin provide structural integrity mostly for the cTECs and mTECs, which form

the epithelioreticular scaffolding essential for T-cell development, while other cytoskeletal components like actin, myosin, and WASP are more critical to thymocyte trafficking, regulating cellular migration and remodeling, processes vital for thymic regeneration[5,66-69]. It should be noted that several of the proteins that were not connected to any network, such as MARCKS-related protein (Marcksl1), are well-established to be involved in the control of cell movement by regulating actin cytoskeleton homeostasis and filipodium/lamellipodium formation[70]. Exclusion of such proteins may be due to the scattered network topology or low-confidence interactions, although their physiology may be highly relevant to the Intermediate Filament Organization cluster. Overall, this cluster reflects dynamic interactions between stromal cells and thymocytes, showcasing the complex, structural and functional remodeling needed to restore thymic homeostasis.

The second cluster, *SRP-Dependent Cotranslational Protein Targeting to Membrane*, includes proteins involved in ribosomal function and protein targeting, such as Ribosomal Protein L23a (Rpl23a), Ribosomal Protein S18 (Rps18), Ribosomal Protein L7a (Rpl7a), Ribosomal Protein L26 (Rpl26), Ribosomal Protein L19 (Rpl19), alongside Pyruvate Kinase M1/2 (Pkm), Shwachman-Bodian-Diamond Syndrome Protein (Sbds), Signal Recognition Particle 54kDa (Srp54b), and Transketolase (Tkt) **(Fig. 6)**. This cluster highlights pathways critical for efficient protein synthesis, folding, and membrane targeting, processes essential for cellular growth and function. In the context of thymic regeneration, these proteins could play a key role in supporting the high metabolic and translational demands of thymic epithelial cells (cTECs and mTECs) and thymocytes during proliferation and differentiation[71,72]. Ribosomal proteins ensure robust protein synthesis, while SRP components may facilitate the translocation of membrane-bound and secretory proteins critical for stromal and immune cell communication[73,74]. Additionally, metabolic regulators like Pkm and Tkt may reflect shifts in cellular energy dynamics, essential for wound healing post-chemotherapy[75,76]. Together, this cluster underscores the functional importance of translational and metabolic machinery in driving thymic repair and structural reorganization.

The third cluster, *RNA Recognition Motif Domain and K Homology Domain Type 1*, includes proteins involved in RNA binding, splicing, and regulation of gene expression, such as Heterogeneous Nuclear Ribonucleoprotein M (Hnrnpm), Hnrnp A/B (Hnrnpab), Hnrnp U-Like 1 (Hnrnpul1), Serine/Arginine-Rich Splicing Factor 2 (Srsf2), Srsf5, ELAV-Like Protein 1 (Elavl1), Thyroid Hormone Receptor-Associated Protein 3 (Thrap3), Pumilio RNA Binding Family Member 60 (Puf60), RAN Binding Protein 1 (Ranbp1), RNA Binding Motif Protein 15 (Rbm15), and Tripartite Motif Containing 28 (Trim28) **(Fig. 6)**. This cluster represents pathways central to post-transcriptional regulation, RNA transport, and alternative splicing, processes essential for the fine-tuned expression of genes required during cellular differentiation and stress responses. In

the context of thymic regeneration, these proteins likely contribute to the adaptive reprogramming of both stromal cells (e.g., cTECs and mTECs) and thymocytes by regulating RNA dynamics and splicing events necessary for cellular proliferation, differentiation, and functional maturation[77]. For instance, Hnrnp and Srsf family members play key roles in RNA processing and alternative splicing, which are crucial for generating the diverse protein repertoire needed during tissue remodeling[78-81]. Proteins like Elavl1 and Trim28 regulate stress responses and chromatin remodeling, processes essential for adapting to the regenerative demands of the thymic microenvironment[82-84]. This cluster highlights the critical role of RNA metabolism in coordinating the molecular programs underlying thymic repair and functional restoration.

Overall, the STRING analysis showcases a complex and dynamic interplay of structural, translational, and post-transcriptional pathways underpinning endogenous thymic regeneration after cyclophosphamide insult. The identified clusters highlight structural remodeling, metabolic adaptability, and RNA regulatory mechanisms, essential for restoring thymic architecture and function, emphasizing the distributed and multifaceted nature of thymic repair processes.

Validation of molecular imaging data from the reconstructed KRT8 signal. To validate our novel PepBridge peak-matching pipeline, we focused on candidate protein markers with known roles in thymic function and homeostasis. One leading candidate peptide was Keratin 8 (KRT8), an intermediate filament, known to define thymic epithelial cells and be expressed in both cTEC and mTEC, regulating thymic homeostasis and regeneration[85-87]. To this end, we used a serial FFPE section of murine thymic tissue, which was cut 5 µm apart from the FFPE sections subjected to MALDI-MSI, thus allowing us to perform co-registration and assess the same regions in both MALDI-MSI and multiplex immunofluorescence **(Figs. 7A-B)**. To better define corticomedullary junctions and map the individual cortical and medullary compartments, we also took advantage of KRT5, an intermediate filament that is exclusively expressed in mTEC[86]. It should be noted that mild changes in tissue morphology are expected, although a generic compartment topology should remain unaltered, when assessing sequential or adjacent tissue sections.

Molecular imaging based on our novel PepBridge scoring system mapped the KRT8 signal in both the cortical and the medullary areas of cyclophosphamide- and vehicle-treated thymi, with higher expression in the medulla, but not in the perithymic stroma or the capsular region **(Fig. 7A-B)**. These findings align well with the expected histological pattern of cTEC and mTEC networks, because cTEC are interconnected in meshwork architecture, in contrast to the more-densely clustered, but individually arranged mTEC[88]. In addition, the perithymic stroma and

capsule are usually composed of loose and dense connective tissue, also including mesenchymal cells, white and brown adipose tissue, which are not expected to express epithelial keratins[8]. When we examined perithymic regions and capsule using KRT5/8 immunofluorescence, we observed minimal or no KRT8 signal **(Figs. 7C-D)**. The thymic capsule, defined by $KRT8^{+}KRT5^{lo}$ cTEC and composed of connective tissue ($DAPI^{+}$) cells, showed no KRT8 expression **(Fig. 7C)**, thus confirming the MALDI-MSI acquisitions in the corresponding region **(Fig. 7A; white box "C")**. In the peri-thymic stroma away from the capsule, specifically in the adjacent brown adipose tissue, we found no KRT8 expression **(Fig. 7D)**, again consistent with the MALDI-MSI data **(Fig. 7B; white box "D")**. In summary, these findings validate the specificity of MALDI-MSI by confirming its ability to detect KRT8 expression exclusively in epithelial regions, with no signal in the $KRT8^{-}$ areas such as the perithymic stroma and capsule.

Shifting our focus to the corticomedullary junctions, we aimed to further assess the accuracy of MALDI-MSI in distinguishing these compartments based on KRT8 distribution. As expected, KRT8 was present in both $KRT5^{-}$ cortical and $KRT5^{+}$ medullary zones, with a marked increase in the latter, as reflected by the distinct topology of these networks (e.g., meshwork vs. dense arrangement) **(Figs. 7E-F)**. Indeed, the corresponding regions in the MALDI-MSI acquisitions showed gradual decrease of the KRT8 molecular signal from medulla to cortex **(Figs. 7A-B; white boxes "E" and "F", respectively)**. Interestingly, we identified certain corticomedullary regions where the KRT8 signal appeared more homogeneously distributed in the MALDI-MSI molecular images **(Figs. 7A-B; white boxes "G" and "H," respectively)**, thus obscuring a clear distinction between the cortical and medullary zones. Upon assessing these regions with KRT5/8 immunofluorescence in detail, we observed a notably thicker and denser cTEC meshwork adjacent to the medulla in these areas **(Figs. 7G-H)**. These corticomedullary regions with uniform KRT8 signal across the boundary were found in both cyclophosphamide- and vehicle-treated mice, although they were more prominent in the former and very rare in control animals **(Figs. 7A-B)**. This pattern likely reflects sites of active cTEC remodeling and regeneration, particularly following cytotoxic chemotherapy, where cTECs respond with rebound hyperplasia to counteract the preceding thymic involution. At this stage, 21 days post-chemotherapy, thymic rebound hyperplasia is expected **(Fig. 1F-H)**. Regardless of their precise origin, the lack of KRT8 signal differentiation in these niches, as detected by MALDI-MSI, underscores its high sensitivity to reveal regions of regenerative activity without distinct compartmental boundaries.

It should be emphasized that the areas selected for immunofluorescence assessment were chosen exclusively based on KRT8 signal perturbations observed in MALDI-MSI acquisitions **(Figs. 7A-B)**. This approach highlighted both the sensitivity and the specificity of MALDI-MSI in

accurately capturing these transition zones, thus validating its capability to delineate subtle shifts in protein expression within the corticomedullary boundary and/or perithymic zones.

Validation of novel thymic compartmentalization markers. Our validation strategy using KRT8 molecular images reinforced the accuracy of our novel scoring system in mapping thymic compartment architecture, as well as in documenting differences between vehicle- and cyclophosphamide-treated thymi. Interestingly however, our strategy has revealed many additional candidates that have never been explored in this context, but could be used either as markers of thymic compartmentalization for mechanistic studies, or as clinical biomarkers of endogenous thymic regeneration and rebound hyperplasia following chemotherapy treatment. Among the 68 candidates, we followed up on Nucleoporin Tpr (TPR), Cysteine and Glycine-Rich Protein-3 (CSPR3), and Tubulin-Specific Chaperone A (TBCA), based on their diversity in expression and distribution within thymic environments.

Nucleoporin TPR is a key component of the nuclear pore complex, with diverse functions, such as RNA export and processing, maintenance of genome stability, and regulation of spindle assembly checkpoint[89-93]. Despite these globally critical roles in cells, the precise spatiotemporal expression and functions of TPR in the human or murine thymus have never been explored. Molecular imaging of TPR via MALDI-MSI revealed clear corticomedullary distinction, with highest levels in the medulla, lower levels in the cortex, and minimal-to-no expression in the capsule and perithymic tissues. In cyclophosphamide-treated animals, however, TPR signal was markedly lost in the medulla and only mildly reduced in the cortex, obscuring the corticomedullary boundaries **(Fig. 8A-A')**. Immunofluorescence analysis of thymi, not imaged by MALDI-MSI, confirmed these findings independently. First, TPR expression was profoundly reduced in the medullas of treated mice compared to controls, and second, cortical levels remained relatively stable **(Figs. 8B-C and 7B'-C')**. At cellular level, TPR was found to be expressed by both mTEC and thymocytes in the medullary region of vehicle-treated animals, but its expression was primarily affected in the thymocytes of treated animals **(Figs 8D-D')**. This reduction in thymocyte-associated TPR likely explains the diminished medullary TPR signal observed in MALDI-MSI molecular images **(Fig. 8A)**, because thymocytes constitute the most abundant cell population in the thymus. Additionally, TPR expression was detected in cTEC and cortical thymocytes, though at lower levels than in the medulla **(Figs. 8D-D')**, again in agreement with MALDI-MSI acquisitions **(Figs. 8A-A')**. Together, these data demonstrate that our pipeline identifies molecules like TPR, whose spatial expression patterns may provide valuable insights into intrathymic remodeling and compartment-specific responses to treatments like cyclophosphamide.

Cysteine and Glycine-Rich Protein-3 (CSRP3) is predominantly expressed in skeletal and cardiac muscle, where it serves as a positive regulator of myogenic differentiation by directly interacting with muscle-specific transcription factors in the nucleus. Additionally, in the cytoplasm, CSRP3 modulates actin remodeling, cell stretching, and calcium signaling[94-97]. CSRP3 levels have been shown to increase in other tissues following injury, particularly in the nervous system, where it aids regeneration, by promoting filopodia formation[98-100]. However, its role in thymus regeneration has not been previously reported. Our results revealed that CSRP3 displays a distribution pattern similar to TPR, with both MALDI-MSI and immunofluorescence showcasing higher expression in the medullary compartment compared to the cortical and perithymic regions **(Figs. 8E-F and 7E'-F')**. Unlike TPR, cyclophosphamide treatment suppressed CSRP3 in both compartments, with a disproportionate and more pronounced decrease in the medullary compartment **(Figs. 8F-G and 7F'-G')**. Consequently, CSRP3 reduction did not obscure the corticomedullary boundaries in treated mice **(Figs. 8E-H and 7E'-H')**. Given the documented role of CSRP3 in tissue regeneration[100], these data suggest that by 3 weeks post-chemotherapy, most intrathymic remodeling has occurred, thus allowing CSRP3 levels to return to baseline. Nonetheless, our MALDI-MSI pipeline was quite sensitive to detect subtle CSRP3 fluctuations, capturing putative finetuning mechanisms supporting thymic remodeling after injury.

Tubulin-Specific Chaperone-A (TBCA) belongs to the five-member family of tubulin-specific chaperones, which function in a concerted fashion with newly synthesized quasi-native tubulin polypeptides to assemble into polymerization-competent heterodimers. Along with other members of the family, TBCA therefore orchestrates an evolutionarily conserved pathway dictating cytoskeletal dynamics and the mitotic spindle apparatus within all cells[101-104]. Although the importance of microtubule dynamics has been recognized in the immune system[105], a detailed analysis on its spatiotemporal expression and function during thymopoiesis is currently lacking. In control animals, TBCA exhibited a distribution pattern similar to TPR and CSRP3, i.e., with higher expression in the medullary compared to the cortical compartment **(Figs. 8I-J and 7I'-J')**. Interestingly, cyclophosphamide-treated mice displayed an increased TBCA expression in the cortex, while the medullary compartment experienced little-to-no decrease, partially obscuring the corticomedullary boundary **(Figs. 8J-K and 7J'-K')**. At the cellular level, the elevated cortical TBCA expression corresponded predominantly to thymocytes **(Figs. 8L-L')**, the primary cell population within the thymus[106]. Given the established roles of TBCA role in regulating microtubule dynamics, partially including assembly of the mitotic spindle during cell division[107], these data align well with the rebound hyperplasia at this stage of our analysis, characterized by ac-

tive thymocyte proliferation and cortical expansion **(Fig. 2H)**. Overall, these data underscore the robustness of our analytical MALDI-MSI pipeline in identifying novel contributors to intrathymic remodeling after injury or stress, as well as in capturing even subtle spatiotemporal changes of protein expression/distribution during the regenerative process.

DISCUSSION

This study introduces a novel pipeline for identifying spatially resolved protein biomarkers in the thymus by integrating MALDI-MSI and LC-MS/MS proteomics. By leveraging the complementary strengths of imaging and proteomics, we successfully mapped protein distribution across distinct thymic compartments and identified biomarkers associated with endogenous thymic regeneration following chemotherapy-induced involution. Our findings reveal significant changes in protein expression patterns within the thymic cortex and medulla during rebound hyperplasia. Key markers, including KRT8, CSRP3, TBCA, and TPR, exhibited distinct spatial distributions and dynamic expression profiles, reflecting critical processes involved in thymic remodeling following chemotherapy insult **(Figs. 7-8)**. Of note, KRT8, a prominent intermediate filament protein, which is well-established to be expressed in both cortical and medullary thymic epithelial cells (cTECs and mTECs)[86,87], displayed a less defined corticomedullary boundaries in cyclophosphamide-treated mice, potentially highlighting defective or ongoing remodeling during the stage of rebound hyperplasia.

Furthermore, our pipeline identified novel markers, such as TBCA, a tubulin-specific chaperone[103], which exhibited increased cortical expression during rebound hyperplasia, suggesting a pivotal role for cytoskeletal remodeling in thymocyte proliferation and cortical expansion. Similarly, TPR, a nuclear pore complex protein[92], demonstrated medullary-specific expression under control conditions but was significantly reduced following cyclophosphamide treatment, particularly in medullary thymocytes, emphasizing their vulnerability to chemotherapeutic insults. Additionally, CSRP3, a protein involved in cytoskeletal remodeling and tissue regeneration[94], displayed higher expression in the medulla compared to the cortex, with cyclophosphamide treatment causing a disproportionate reduction in the medullary compartment. These findings highlight the potential of TBCA, TPR, and CSRP3 as key markers for thymic compartmentalization and regeneration. Beyond identifying previously underrecognized factors of thymic remodeling, this study is the first to present a spatiotemporally characterized proteome of thymic compartmentalization and recovery. To our knowledge, MALDI-MSI approaches have never before been applied to the thymus, let alone combined with LC-MS/MS proteomics in such a sophisticated and integrative manner. This innovative combination enabled high-confidence protein mapping across thymic compartments, yielding unprecedented spatial resolution of proteomic changes. By leveraging the strengths of both technologies, this approach provides not only a detailed atlas of thymic proteins but also a framework for future studies to explore complex tissue dynamics with enhanced precision and reliability. These advancements position this study as a significant methodological leap forward in understanding thymic regeneration.

Immune and thymic recovery post-chemotherapy is a critical clinical challenge, particularly in pediatric cancer patients, who often experience long-term immune dysfunction due to chemotherapy-induced thymic involution. The thymus plays a central role in T-cell development, and its damage can lead to impaired thymopoiesis, diminished T-cell output, and compromised immune reconstitution. This creates a vulnerability to infections, secondary malignancies, and inadequate immune surveillance, which are significant contributors to morbidity and mortality in pediatric cancer survivors[35]. Studies like this one address this critical need by providing foundational insights into molecular mechanisms of thymic regeneration, offering potential therapeutic targets and/or functional biomarkers of thymopoiesis. While it is unlikely that MALDI-MSI coupled with LC-MS/MS will be directly implemented in clinical care for pediatric cancer patients—given that thymic biopsy is highly invasive and not part of standard management—this technology holds great promise in preclinical settings. It could be employed to establish pharmacodynamic biomarkers to monitor immune recovery during cytotoxic treatments in preclinical mouse models[108], thereby enhancing the discovery of novel drugs or drug combinations aimed at achieving immunological/thymic recovery post-chemotherapy. For example, proteins such as TBCA, TPR, and CSRP3, identified in this study and implicated in cytoskeletal remodeling, compartmental stability, and thymic regeneration, could serve as biomarkers for monitoring thymic recovery following cyclophosphamide treatment in animal research. Cyclophosphamide remains a cornerstone chemotherapeutic agent in the management of pediatric malignancies[109-111], and leveraging such biomarkers in preclinical models could provide critical insights to optimize therapeutic strategies and improve long-term immune outcomes for pediatric patients.

The versatility of this spatial proteomics platform extends well beyond its application in thymic compartmentalization. The integration of MALDI-MSI with LC-MS/MS proteomics offers a robust framework for identifying spatially resolved protein markers across all lymphoid organs, including lymph nodes, spleen, thymus, and bone marrow. These organs play pivotal roles in immune surveillance, host-pathogen interactions, and hematopoiesis, and their compartmentalization is critical for orchestrating immune responses[44,112-115]. By mapping the spatial proteome of these tissues, our approach uncovers biomarkers and signaling pathways mediating immune-host cell interactions, providing invaluable insights into both physiological and pathological immune-related processes. Advancements in spatial proteomics beyond laser-capture microdissection, have already begun to illuminate key aspects of tissue organization and functionality in lymphoid organs. For instance, one study has employed MALDI-TOF MSI in tracheobronchial lymph nodes revealing the spatial distribution of interleukins and other immune mediators in pigs after respiratory infection[116]. In another study, MALDI-MSI was employed in lymph

nodes of primary endometrial cancers, and successfully identified discriminators of metastasis through mapping *m/z* values corresponding to alpha-Actin-2 and plectin[117]. MALDI-MSI has been applied to mouse spleens in a model of splenic injury, though a lipidomic rather than a proteomic pipeline was utilized to characterize the immunotoxic effects of bisphenol S[118]. Despite these advances, challenges remain in achieving high-resolution protein mapping within complex tissue architectures. The combination of MALDI-MSI with LC-MS/MS, as demonstrated in our study, represents a significant leap forward by enabling high-confidence protein identification with spatial context. Applying this technology to other lymphoid organs could provide detailed atlases of proteomic landscapes, allowing researchers to pinpoint alterations in tissue organization, and immune interactions under conditions such as infection, autoimmunity, and cancer.

To address MALDI-TOF's low spectral resolution and improve peptide identification, we developed the Pep-Bridge scoring pipeline, which reduces ambiguity in peptide assignments but requires larger datasets and machine learning-driven automation for full implementation. Currently, the limited number of MALDI-MSI images restricts the creation of robust training sets for these computational approaches. Although several on-tissue bottom-up proteomics studies have combined peptide spatial mapping by MALDI-MSI with LC-MS/MS to identify protein markers from tissue sections[119-125], there is still no streamlined method for directly correlating these datasets. MALDI-IHC, a recent innovation, integrates MALDI-MSI with immunohistochemistry by employing photocleavable mass-tagged antibodies and laser capture microdissection to localize and quantify targeted antigens, followed by downstream LC-MS/MS analyses. However, this targeted approach relies on known antigens, which can be truncated or mutated in disease states, potentially limiting its applicability. We anticipate that complementing MALDI-IHC with unbiased strategies—specifically automated pipelines augmented by scoring systems and machine learning—will enable direct matching of thousands of bottom-up derived peptides or proteins to MALDI-MSI images, closing a critical gap in comprehensive tissue-based proteomic studies.

In conclusion, this study establishes a groundbreaking spatial proteomics pipeline that not only advances our understanding of thymic regeneration but also lays the foundation for broader applications across lymphoid organs. By combining MALDI-MSI and LC-MS/MS with high-confidence protein mapping, this platform offers unparalleled insights into tissue compartmentalization and immune interactions, with the potential to inform therapeutic strategies and improve immune recovery in diverse pathological contexts.

Raw data availability

The mass spectrometry data have been deposited to the ProteomeXchange Consortium via the PRIDE partner repository with the dataset identifier PXD058296. For reviewers to access this dataset please use the token: YhaGeXAUR9tx. Alternatively, reviewers can access the dataset by logging in to the PRIDE website using the following account details:
Username: reviewer_pxd058296@ebi.ac.uk. Password: GZtW9DnfvbEr.

Acknowledgments

The Karagiannis Lab gratefully acknowledges the Montefiore-Einstein Comprehensive Cancer Center for funding through its support grant (P30 CA013330), as well as the Analytical Imaging Facility and its dedicated personnel for the use of the Fast Scanner, acquired via shared instrumentation grants (1S10 OD026852-01A1). The Sidoli Lab gratefully acknowledges funding from the Hevolution Foundation (AFAR), the Einstein-Mount Sinai Diabetes Center, and the NIH Office of the Director (S10 OD030286).

Conflict of interest statement

The authors declare no financial conflicts of interest.

REFERENCES

1 Mund, A. *et al.* Deep Visual Proteomics defines single-cell identity and heterogeneity. *Nat Biotechnol* **40**, 1231-1240 (2022). https://doi.org:10.1038/s41587-022-01302-5

2 Gonzalez-Fernandez, A., Dexter, A., Nikula, C. J. & Bunch, J. NECTAR: A New Algorithm for Characterizing and Correcting Noise in QToF-Mass Spectrometry Imaging Data. *J Am Soc Mass Spectrom* **34**, 2443-2453 (2023). https://doi.org:10.1021/jasms.3c00116

3 Buchberger, A. R., DeLaney, K., Johnson, J. & Li, L. Mass Spectrometry Imaging: A Review of Emerging Advancements and Future Insights. *Anal Chem* **90**, 240-265 (2018). https://doi.org:10.1021/acs.analchem.7b04733

4 Hun, M. L. *et al.* Gender Disparity Impacts on Thymus Aging and LHRH Receptor Antagonist-Induced Thymic Reconstitution Following Chemotherapeutic Damage. *Front Immunol* **11**, 302 (2020). https://doi.org:10.3389/fimmu.2020.00302

5 Kadouri, N., Nevo, S., Goldfarb, Y. & Abramson, J. Thymic epithelial cell heterogeneity: TEC by TEC. *Nat Rev Immunol* **20**, 239-253 (2020). https://doi.org:10.1038/s41577-019-0238-0

6 Manley, N. R., Richie, E. R., Blackburn, C. C., Condie, B. G. & Sage, J. Structure and function of the thymic microenvironment. *Front Biosci (Landmark Ed)* **16**, 2461-2477 (2011). https://doi.org:10.2741/3866

7 Han, J. & Zuniga-Pflucker, J. C. A 2020 View of Thymus Stromal Cells in T Cell Development. *J Immunol* **206**, 249-256 (2021). https://doi.org:10.4049/jimmunol.2000889

8 James, K. D., Jenkinson, W. E. & Anderson, G. Non-Epithelial Stromal Cells in Thymus Development and Function. *Front Immunol* **12**, 634367 (2021). https://doi.org:10.3389/fimmu.2021.634367

9 Bhalla, P., Su, D. M. & van Oers, N. S. C. Thymus Functionality Needs More Than a Few TECs. *Front Immunol* **13**, 864777 (2022). https://doi.org:10.3389/fimmu.2022.864777

10 Nitta, T. Mesenchymal stromal cells in the thymus. *Inflamm Regen* **42**, 33 (2022). https://doi.org:10.1186/s41232-022-00219-5

11 Owen, J. J., McLoughlin, D. E., Suniara, R. K. & Jenkinson, E. J. The role of mesenchyme in thymus development. *Curr Top Microbiol Immunol* **251**, 133-137 (2000). https://doi.org:10.1007/978-3-642-57276-0_17

12 Abramson, J. & Anderson, G. Thymic Epithelial Cells. *Annu Rev Immunol* **35**, 85-118 (2017). https://doi.org:10.1146/annurev-immunol-051116-052320

13 Alawam, A. S., Anderson, G. & Lucas, B. Generation and Regeneration of Thymic Epithelial Cells. *Front Immunol* **11**, 858 (2020). https://doi.org:10.3389/fimmu.2020.00858

14 Anderson, G. & Takahama, Y. Thymic epithelial cells: working class heroes for T cell development and repertoire selection. *Trends Immunol* **33**, 256-263 (2012). https://doi.org:10.1016/j.it.2012.03.005

15 Cabric, V. & Brown, C. C. Thymic mimicry: The art of imitation. *J Exp Med* **220** (2023). https://doi.org:10.1084/jem.20231010

16 Chidgey, A. P. & Boyd, R. L. Thymic stromal cells and positive selection. *APMIS* **109**, 481-492 (2001). https://doi.org:10.1111/j.1600-0463.2001.apm090701.x

17 Kato, S. Thymic microvascular system. *Microsc Res Tech* **38**, 287-299 (1997). https://doi.org:10.1002/(SICI)1097-0029(19970801)38:3<287::AID-JEMT9>3.0.CO;2-J

18 Munoz, J. J. *et al.* Organizing the thymus gland. *Ann N Y Acad Sci* **1153**, 14-19 (2009). https://doi.org:10.1111/j.1749-6632.2008.03965.x

19 Takahama, Y., Ohigashi, I., Baik, S. & Anderson, G. Generation of diversity in thymic epithelial cells. *Nat Rev Immunol* **17**, 295-305 (2017). https://doi.org:10.1038/nri.2017.12

20 Sun, Q., Tiziana, P., Khan, A. U. M., Heuveline, V. & Gretz, N. A simple optical tissue clearing pipeline for 3D vasculature imaging of the mediastinal organs in mice. *Int J Exp Pathol* **102**, 218-227 (2021). https://doi.org:10.1111/iep.12399

21 Cahill, R. N., Kimpton, W. G., Cunningham, C. P. & Washington, E. A. An immune system switch at birth triggers a change in the lifespan of peripheral T cells. *Semin Immunol* **9**, 355-363 (1997). https://doi.org:10.1006/smim.1997.0093
22 Webb, S. & Haniffa, M. Large-scale single-cell RNA sequencing atlases of human immune cells across lifespan: Possibilities and challenges. *Eur J Immunol*, e2250222 (2023). https://doi.org:10.1002/eji.202250222
23 Baran-Gale, J. *et al.* Ageing compromises mouse thymus function and remodels epithelial cell differentiation. *Elife* **9** (2020). https://doi.org:10.7554/eLife.56221
24 Minato, N., Hattori, M. & Hamazaki, Y. Physiology and pathology of T-cell aging. *Int Immunol* **32**, 223-231 (2020). https://doi.org:10.1093/intimm/dxaa006
25 Ostan, R. *et al.* Immunosenescence and immunogenetics of human longevity. *Neuroimmunomodulation* **15**, 224-240 (2008). https://doi.org:10.1159/000156466
26 Palmer, S., Albergante, L., Blackburn, C. C. & Newman, T. J. Thymic involution and rising disease incidence with age. *Proc Natl Acad Sci U S A* **115**, 1883-1888 (2018). https://doi.org:10.1073/pnas.1714478115
27 Aw, D., Silva, A. B. & Palmer, D. B. Is thymocyte development functional in the aged? *Aging (Albany NY)* **1**, 146-153 (2009). https://doi.org:10.18632/aging.100027
28 Palmer, D. B. The effect of age on thymic function. *Front Immunol* **4**, 316 (2013). https://doi.org:10.3389/fimmu.2013.00316
29 Rane, S., Hogan, T., Lee, E., Seddon, B. & Yates, A. J. Towards a unified model of naive T cell dynamics across the lifespan. *Elife* **11** (2022). https://doi.org:10.7554/eLife.78168
30 Ansari, A. R. & Liu, H. Acute Thymic Involution and Mechanisms for Recovery. *Arch Immunol Ther Exp (Warsz)* **65**, 401-420 (2017). https://doi.org:10.1007/s00005-017-0462-x
31 Kinsella, S. & Dudakov, J. A. When the Damage Is Done: Injury and Repair in Thymus Function. *Front Immunol* **11**, 1745 (2020). https://doi.org:10.3389/fimmu.2020.01745
32 Swami, S., Tong, I., Bilodeau, C. C. & Bourjeily, G. Thymic involution in pregnancy: a universal finding? *Obstet Med* **5**, 130-132 (2012). https://doi.org:10.1258/om.2011.110077
33 Yang, H. *et al.* Obesity accelerates thymic aging. *Blood* **114**, 3803-3812 (2009). https://doi.org:10.1182/blood-2009-03-213595
34 Chaudhry, M. S., Velardi, E., Dudakov, J. A. & van den Brink, M. R. Thymus: the next (re)generation. *Immunol Rev* **271**, 56-71 (2016). https://doi.org:10.1111/imr.12418
35 Lagou, M. K., Anastasiadou, D. P. & Karagiannis, G. S. A Proposed Link Between Acute Thymic Involution and Late Adverse Effects of Chemotherapy. *Front Immunol* **13**, 933547 (2022). https://doi.org:10.3389/fimmu.2022.933547
36 Wertheimer, T. *et al.* Production of BMP4 by endothelial cells is crucial for endogenous thymic regeneration. *Sci Immunol* **3** (2018). https://doi.org:10.1126/sciimmunol.aal2736
37 Fletcher, A. L. *et al.* Ablation and regeneration of tolerance-inducing medullary thymic epithelial cells after cyclosporine, cyclophosphamide, and dexamethasone treatment. *J Immunol* **183**, 823-831 (2009). https://doi.org:10.4049/jimmunol.0900225
38 Szklarczyk, D. *et al.* The STRING database in 2023: protein-protein association networks and functional enrichment analyses for any sequenced genome of interest. *Nucleic Acids Res* **51**, D638-D646 (2023). https://doi.org:10.1093/nar/gkac1000
39 Karagiannis, G. S. *et al.* Neoadjuvant chemotherapy induces breast cancer metastasis through a TMEM-mediated mechanism. *Science Translational Medicine* **9** (2017). https://doi.org:10.1126/scitranslmed.aan0026
40 Borriello, L. *et al.* The role of the tumor microenvironment in tumor cell intravasation and dissemination. *Eur J Cell Biol* **99**, 151098 (2020). https://doi.org:10.1016/j.ejcb.2020.151098
41 Coste, A. *et al.* Hematogenous Dissemination of Breast Cancer Cells From Lymph Nodes Is Mediated by Tumor MicroEnvironment of Metastasis Doorways. *Front Oncol* **10**, 571100 (2020). https://doi.org:10.3389/fonc.2020.571100

42 Sharma, V. P. *et al.* Live tumor imaging shows macrophage induction and TMEM-mediated enrichment of cancer stem cells during metastatic dissemination. *Nat Commun* **12**, 7300 (2021). https://doi.org:10.1038/s41467-021-27308-2
43 Moll, U. M. Functional histology of the neuroendocrine thymus. *Microsc Res Tech* **38**, 300-310 (1997). https://doi.org:10.1002/(SICI)1097-0029(19970801)38:3<300::AID-JEMT10>3.0.CO;2-R
44 Pearse, G. Normal structure, function and histology of the thymus. *Toxicol Pathol* **34**, 504-514 (2006). https://doi.org:10.1080/01926230600865549
45 Perez, Y. E. & Moran, C. A. The thymus: General concepts on embryology, anatomy, histology and immunohistochemistry. *Semin Diagn Pathol* **39**, 86-91 (2022). https://doi.org:10.1053/j.semdp.2021.06.003
46 Suster, S. & Rosai, J. Histology of the normal thymus. *Am J Surg Pathol* **14**, 284-303 (1990). https://doi.org:10.1097/00000478-199003000-00010
47 Kahri, A. I., Salmi, A., Hannuksela, M. & Karaharju, E. O. Histochemistry of rat thymus during involution induced by alkylating agents. *Acta Pathol Microbiol Scand* **64**, 441-449 (1965). https://doi.org:10.1111/apm.1965.64.4.441
48 Anton, E. Delayed toxicity of cyclophosphamide in normal mice. *Br J Exp Pathol* **68**, 237-249 (1987).
49 Yoon, S., Yoo, Y. H., Kim, B. S. & Kim, J. J. Ultrastructural alterations of the cortical epithelial cells of the rat thymus after cyclophosphamide treatment. *Histol Histopathol* **12**, 401-413 (1997).
50 Basta-Kaim, A., Kubera, M., Budziszewska, B., Roman, A. & Skowron-Cendrzak, A. Effect of physiological and pharmacologically induced thymus involution on the immunoreactivity in C57BL mice. *Pol J Pharmacol* **53**, 403-407 (2001).
51 Erokhina, V. & Avilova, O. Ultramicroscopic changes of rats parathyroid glands and thymus after single administration of cyclophosphamide at the different periods of observation. *Wiad Lek* **72**, 362-367 (2019).
52 Dudakov, J. A. *et al.* Interleukin-22 drives endogenous thymic regeneration in mice. *Science* **336**, 91-95 (2012). https://doi.org:10.1126/science.1218004
53 Zhan, Y. *et al.* The Reparative Effects of Human Adipose-Derived Mesenchymal Stem Cells in the Chemotherapy-Damaged Thymus. *Stem Cells Dev* **28**, 186-195 (2019). https://doi.org:10.1089/scd.2018.0142
54 Arpaci, T. & Karagun, B. S. Rebound thymic hyperplasia after bone marrow transplantation in children with haemato-oncological diseases. *Contemp Oncol (Pozn)* **22**, 95-98 (2018). https://doi.org:10.5114/wo.2018.75398
55 Ayyildiz, V., Koksal, A. & Ogul, Y. Rebound Thymic Hyperplasia Secondary to Surgical Therapy of Parotid Tumor. *Arch Bronconeumol* **58**, 509 (2022). https://doi.org:10.1016/j.arbres.2021.06.014
56 Chen, C. H. *et al.* Rebound Thymic Hyperplasia after Chemotherapy in Children with Lymphoma. *Pediatr Neonatol* **58**, 151-157 (2017). https://doi.org:10.1016/j.pedneo.2016.02.007
57 Deniz, S. *et al.* Effect of Rebound Thymic Hyperplasia on Survival in Chemotherapy-Treated Lung Cancer. *Turk Thorac J* **21**, 303-307 (2020). https://doi.org:10.5152/TurkThoracJ.2020.18163
58 Franke, F. C. *et al.* Differentiation between rebound thymic hyperplasia and thymic relapse after chemotherapy in pediatric Hodgkin lymphoma. *Pediatr Blood Cancer* **70**, e30421 (2023). https://doi.org:10.1002/pbc.30421
59 Gulati, N. & Giulino-Roth, L. Do no harm: Distinguishing between rebound thymic hyperplasia and Hodgkin lymphoma relapse in children. *Pediatr Blood Cancer* **70**, e30492 (2023). https://doi.org:10.1002/pbc.30492

60 Lazaro-Garcia, A. *et al.* Post-Chemotherapy Rebound Thymic Hyperplasia Mimicking Relapse in Breast Implant-Associated Anaplastic Large Cell Lymphoma: A Case Report. *Oncol Res Treat* **44**, 196-200 (2021). https://doi.org:10.1159/000515055
61 Qiu, L. *et al.* Thymic rebound hyperplasia post-chemotherapy mistaken as disease progression in a patient with lymphoma involving mediastinum: a case report and reflection. *BMC Surg* **21**, 38 (2021). https://doi.org:10.1186/s12893-021-01048-y
62 Sun, D. P. *et al.* Thymic hyperplasia after chemotherapy in adults with mature B cell lymphoma and its influence on thymic output and CD4(+) T cells repopulation. *Oncoimmunology* **5**, e1137417 (2016). https://doi.org:10.1080/2162402X.2015.1137417
63 Goldberg, G. L. *et al.* Sex steroid ablation enhances immune reconstitution following cytotoxic antineoplastic therapy in young mice. *J Immunol* **184**, 6014-6024 (2010). https://doi.org:10.4049/jimmunol.0802445
64 Sun, L. *et al.* FSP1(+) fibroblast subpopulation is essential for the maintenance and regeneration of medullary thymic epithelial cells. *Sci Rep* **5**, 14871 (2015). https://doi.org:10.1038/srep14871
65 Velardi, E., Tsai, J. J. & van den Brink, M. R. M. T cell regeneration after immunological injury. *Nat Rev Immunol* **21**, 277-291 (2021). https://doi.org:10.1038/s41577-020-00457-z
66 Thompson, S. B., Waldman, M. M. & Jacobelli, J. Polymerization power: effectors of actin polymerization as regulators of T lymphocyte migration through complex environments. *FEBS J* **289**, 6154-6171 (2022). https://doi.org:10.1111/febs.16130
67 Serrador, J. M., Nieto, M. & Sanchez-Madrid, F. Cytoskeletal rearrangement during migration and activation of T lymphocytes. *Trends Cell Biol* **9**, 228-233 (1999). https://doi.org:10.1016/s0962-8924(99)01553-6
68 Kuznetsov, N. V. *et al.* Nuclear Wiskott-Aldrich syndrome protein co-regulates T cell factor 1-mediated transcription in T cells. *Genome Med* **9**, 91 (2017). https://doi.org:10.1186/s13073-017-0481-6
69 Ahmad Mokhtar, A. M. *et al.* RhoG's Role in T Cell Activation and Function. *Front Immunol* **13**, 845064 (2022). https://doi.org:10.3389/fimmu.2022.845064
70 El Amri, M., Fitzgerald, U. & Schlosser, G. MARCKS and MARCKS-like proteins in development and regeneration. *J Biomed Sci* **25**, 43 (2018). https://doi.org:10.1186/s12929-018-0445-1
71 Marchingo, J. M. & Cantrell, D. A. Protein synthesis, degradation, and energy metabolism in T cell immunity. *Cell Mol Immunol* **19**, 303-315 (2022). https://doi.org:10.1038/s41423-021-00792-8
72 Sun, V. *et al.* The Metabolic Landscape of Thymic T Cell Development In Vivo and In Vitro. *Front Immunol* **12**, 716661 (2021). https://doi.org:10.3389/fimmu.2021.716661
73 Goscinska, K. & Topf, U. The evolving role of ribosomes in the regulation of protein synthesis. *Acta Biochim Pol* **67**, 465-473 (2020). https://doi.org:10.18388/abp.2020_5384
74 Sedwick, C. SRP and NAC: guiding a nascent protein's first steps. *PLoS Biol* **9**, e1001103 (2011). https://doi.org:10.1371/journal.pbio.1001103
75 Im, M. J. & Hoopes, J. E. Transketolase and transaldolase activities in regenerating epithelium during wound healing. *J Surg Res* **25**, 50-53 (1978). https://doi.org:10.1016/0022-4804(78)90157-9
76 Kim, E. *et al.* Pyruvate Kinase M2 Accelerates Cutaneous Wound Healing via Glycolysis and Wnt/beta-Catenin Signaling. *Pharmaceutics* **15** (2023). https://doi.org:10.3390/pharmaceutics15082028
77 Le, J. *et al.* Single-Cell RNA-Seq Mapping of Human Thymopoiesis Reveals Lineage Specification Trajectories and a Commitment Spectrum in T Cell Development. *Immunity* **52**, 1105-1118 e1109 (2020). https://doi.org:10.1016/j.immuni.2020.05.010

78 Thibault, P. A. *et al.* hnRNP A/B Proteins: An Encyclopedic Assessment of Their Roles in Homeostasis and Disease. *Biology (Basel)* **10** (2021). https://doi.org:10.3390/biology10080712
79 Zhang, H., Zhu, H., Peng, H. & Sheng, Y. Function of serine/arginine-rich splicing factors in hematopoiesis and hematopoietic malignancies. *Cancer Cell Int* **24**, 257 (2024). https://doi.org:10.1186/s12935-024-03438-7
80 Qi, Z. *et al.* SRSF1 serves as a critical posttranscriptional regulator at the late stage of thymocyte development. *Sci Adv* **7** (2021). https://doi.org:10.1126/sciadv.abf0753
81 Geuens, T., Bouhy, D. & Timmerman, V. The hnRNP family: insights into their role in health and disease. *Hum Genet* **135**, 851-867 (2016). https://doi.org:10.1007/s00439-016-1683-5
82 Ghosh, M. *et al.* Essential role of the RNA-binding protein HuR in progenitor cell survival in mice. *J Clin Invest* **119**, 3530-3543 (2009). https://doi.org:10.1172/JCI38263
83 Papadaki, O. *et al.* Control of thymic T cell maturation, deletion and egress by the RNA-binding protein HuR. *J Immunol* **182**, 6779-6788 (2009). https://doi.org:10.4049/jimmunol.0900377
84 Zhou, X. F. *et al.* TRIM28 mediates chromatin modifications at the TCRalpha enhancer and regulates the development of T and natural killer T cells. *Proc Natl Acad Sci U S A* **109**, 20083-20088 (2012). https://doi.org:10.1073/pnas.1214704109
85 Odaka, C. *et al.* Keratin 8 is required for the maintenance of architectural structure in thymus epithelium. *PLoS One* **8**, e75101 (2013). https://doi.org:10.1371/journal.pone.0075101
86 Lee, E. N. *et al.* Characterization of the expression of cytokeratins 5, 8, and 14 in mouse thymic epithelial cells during thymus regeneration following acute thymic involution. *Anat Cell Biol* **44**, 14-24 (2011). https://doi.org:10.5115/acb.2011.44.1.14
87 Gupta, R. *et al.* Cytokeratin (CK5, CK8, CK14) expression and presence of progenitor stem cells in human fetal thymuses. *Clin Anat* **29**, 711-717 (2016). https://doi.org:10.1002/ca.22736
88 Lagou, M. K. *et al.* Morphometric Analysis of the Thymic Epithelial Cell (TEC) Network Using Integrated and Orthogonal Digital Pathology Approaches. *bioRxiv* (2024). https://doi.org:10.1101/2024.03.11.584509
89 Bermejo, R. *et al.* The replication checkpoint protects fork stability by releasing transcribed genes from nuclear pores. *Cell* **146**, 233-246 (2011). https://doi.org:10.1016/j.cell.2011.06.033
90 Garcia-Benitez, F., Gaillard, H. & Aguilera, A. Physical proximity of chromatin to nuclear pores prevents harmful R loop accumulation contributing to maintain genome stability. *Proc Natl Acad Sci U S A* **114**, 10942-10947 (2017). https://doi.org:10.1073/pnas.1707845114
91 Lee, S. H., Sterling, H., Burlingame, A. & McCormick, F. Tpr directly binds to Mad1 and Mad2 and is important for the Mad1-Mad2-mediated mitotic spindle checkpoint. *Genes Dev* **22**, 2926-2931 (2008). https://doi.org:10.1101/gad.1677208
92 Krull, S. *et al.* Protein Tpr is required for establishing nuclear pore-associated zones of heterochromatin exclusion. *EMBO J* **29**, 1659-1673 (2010). https://doi.org:10.1038/emboj.2010.54
93 Rajanala, K. & Nandicoori, V. K. Localization of nucleoporin Tpr to the nuclear pore complex is essential for Tpr mediated regulation of the export of unspliced RNA. *PLoS One* **7**, e29921 (2012). https://doi.org:10.1371/journal.pone.0029921
94 Vafiadaki, E. *et al.* Muscle lim protein isoform negatively regulates striated muscle actin dynamics and differentiation. *FEBS J* **281**, 3261-3279 (2014). https://doi.org:10.1111/febs.12859
95 Heineke, J. *et al.* Attenuation of cardiac remodeling after myocardial infarction by muscle LIM protein-calcineurin signaling at the sarcomeric Z-disc. *Proc Natl Acad Sci U S A* **102**, 1655-1660 (2005). https://doi.org:10.1073/pnas.0405488102

96 Gehmlich, K., Geier, C., Milting, H., Furst, D. & Ehler, E. Back to square one: what do we know about the functions of muscle LIM protein in the heart? *J Muscle Res Cell Motil* **29**, 155-158 (2008). https://doi.org:10.1007/s10974-008-9159-4
97 Kong, Y., Flick, M. J., Kudla, A. J. & Konieczny, S. F. Muscle LIM protein promotes myogenesis by enhancing the activity of MyoD. *Mol Cell Biol* **17**, 4750-4760 (1997). https://doi.org:10.1128/MCB.17.8.4750
98 Levin, E. *et al.* Muscle LIM Protein Is Expressed in the Injured Adult CNS and Promotes Axon Regeneration. *Cell Rep* **26**, 1021-1032 e1026 (2019). https://doi.org:10.1016/j.celrep.2018.12.026
99 Levin, E., Leibinger, M., Andreadaki, A. & Fischer, D. Neuronal expression of muscle LIM protein in postnatal retinae of rodents. *PLoS One* **9**, e100756 (2014). https://doi.org:10.1371/journal.pone.0100756
100 Levin, E., Andreadaki, A., Gobrecht, P., Bosse, F. & Fischer, D. Nociceptive DRG neurons express muscle lim protein upon axonal injury. *Sci Rep* **7**, 643 (2017). https://doi.org:10.1038/s41598-017-00590-1
101 Tian, G., Vainberg, I. E., Tap, W. D., Lewis, S. A. & Cowan, N. J. Quasi-native chaperonin-bound intermediates in facilitated protein folding. *J Biol Chem* **270**, 23910-23913 (1995). https://doi.org:10.1074/jbc.270.41.23910
102 Tian, G. *et al.* Tubulin subunits exist in an activated conformational state generated and maintained by protein cofactors. *J Cell Biol* **138**, 821-832 (1997). https://doi.org:10.1083/jcb.138.4.821
103 Cowan, N. J. & Lewis, S. A. Type II chaperonins, prefoldin, and the tubulin-specific chaperones. *Adv Protein Chem* **59**, 73-104 (2001). https://doi.org:10.1016/s0065-3233(01)59003-8
104 Bhamidipati, A., Lewis, S. A. & Cowan, N. J. ADP ribosylation factor-like protein 2 (Arl2) regulates the interaction of tubulin-folding cofactor D with native tubulin. *J Cell Biol* **149**, 1087-1096 (2000). https://doi.org:10.1083/jcb.149.5.1087
105 Binarova, P. & Tuszynski, J. Tubulin: Structure, Functions and Roles in Disease. *Cells* **8** (2019). https://doi.org:10.3390/cells8101294
106 Granadier, D., Iovino, L., Kinsella, S. & Dudakov, J. A. Dynamics of thymus function and T cell receptor repertoire breadth in health and disease. *Semin Immunopathol* **43**, 119-134 (2021). https://doi.org:10.1007/s00281-021-00840-5
107 Fanarraga, M. L., Bellido, J., Jaen, C., Villegas, J. C. & Zabala, J. C. TBCD links centriologenesis, spindle microtubule dynamics, and midbody abscission in human cells. *PLoS One* **5**, e8846 (2010). https://doi.org:10.1371/journal.pone.0008846
108 Califf, R. M. Biomarker definitions and their applications. *Exp Biol Med (Maywood)* **243**, 213-221 (2018). https://doi.org:10.1177/1535370217750088
109 Gilheeney, S. W. *et al.* A phase II trial of thalidomide and cyclophosphamide in patients with recurrent or refractory pediatric malignancies. *Pediatr Blood Cancer* **49**, 261-265 (2007). https://doi.org:10.1002/pbc.21045
110 Yanagisawa, R. *et al.* Low toxicity of a conditioning with 8-Gy total body irradiation, fludarabine and cyclophosphamide as preparative regimen for allogeneic hematopoietic stem cell transplantation in pediatric hematological malignancies. *Pediatr Transplant* **13**, 737-745 (2009). https://doi.org:10.1111/j.1399-3046.2008.01065.x
111 El Kababri, M. *et al.* Metro-SMHOP 01: Metronomics combination with cyclophosphamide-etoposide and valproic acid for refractory and relapsing pediatric malignancies. *Pediatr Blood Cancer* **67**, e28508 (2020). https://doi.org:10.1002/pbc.28508
112 Cesta, M. F. Normal structure, function, and histology of mucosa-associated lymphoid tissue. *Toxicol Pathol* **34**, 599-608 (2006). https://doi.org:10.1080/01926230600865531
113 Cesta, M. F. Normal structure, function, and histology of the spleen. *Toxicol Pathol* **34**, 455-465 (2006). https://doi.org:10.1080/01926230600867743

114 Travlos, G. S. Normal structure, function, and histology of the bone marrow. *Toxicol Pathol* **34**, 548-565 (2006). https://doi.org:10.1080/01926230600939856
115 Willard-Mack, C. L. Normal structure, function, and histology of lymph nodes. *Toxicol Pathol* **34**, 409-424 (2006). https://doi.org:10.1080/01926230600867727
116 Do, T. *et al.* MALDI MSI Reveals the Spatial Distribution of Protein Markers in Tracheobronchial Lymph Nodes and Lung of Pigs after Respiratory Infection. *Molecules* **25** (2020). https://doi.org:10.3390/molecules25235723
117 Mittal, P. *et al.* Lymph node metastasis of primary endometrial cancers: Associated proteins revealed by MALDI imaging. *Proteomics* **16**, 1793-1801 (2016). https://doi.org:10.1002/pmic.201500455
118 Zhao, C. *et al.* Evaluation of the splenic injury following exposure of mice to bisphenol S: A mass spectrometry-based lipidomics and imaging analysis. *Environ Int* **135**, 105378 (2020). https://doi.org:10.1016/j.envint.2019.105378
119 Deininger, S. O. *et al.* Normalization in MALDI-TOF imaging datasets of proteins: practical considerations. *Anal Bioanal Chem* **401**, 167-181 (2011). https://doi.org:10.1007/s00216-011-4929-z
120 Lagarrigue, M. *et al.* Revisiting rat spermatogenesis with MALDI imaging at 20-microm resolution. *Mol Cell Proteomics* **10**, M110 005991 (2011). https://doi.org:10.1074/mcp.M110.005991
121 Rauser, S., Deininger, S. O., Suckau, D., Hofler, H. & Walch, A. Approaching MALDI molecular imaging for clinical proteomic research: current state and fields of application. *Expert Rev Proteomics* **7**, 927-941 (2010). https://doi.org:10.1586/epr.10.83
122 Rauser, S. *et al.* Classification of HER2 receptor status in breast cancer tissues by MALDI imaging mass spectrometry. *J Proteome Res* **9**, 1854-1863 (2010). https://doi.org:10.1021/pr901008d
123 Walch, A., Rauser, S., Deininger, S. O. & Hofler, H. MALDI imaging mass spectrometry for direct tissue analysis: a new frontier for molecular histology. *Histochem Cell Biol* **130**, 421-434 (2008). https://doi.org:10.1007/s00418-008-0469-9
124 Angel, P. M. *et al.* Mapping Extracellular Matrix Proteins in Formalin-Fixed, Paraffin-Embedded Tissues by MALDI Imaging Mass Spectrometry. *J Proteome Res* **17**, 635-646 (2018). https://doi.org:10.1021/acs.jproteome.7b00713
125 Franck, J. *et al.* MALDI imaging mass spectrometry: state of the art technology in clinical proteomics. *Mol Cell Proteomics* **8**, 2023-2033 (2009). https://doi.org:10.1074/mcp.R800016-MCP200

Figure Legends

Figure 1. Workflow for spatial proteomics analysis of thymic tissues combining MALDI-MSI and LC-MS/MS. (A) Thymic FFPE tissue sections were prepared for MALDI-MSI analysis, including deparaffinization, enzymatic digestion, and matrix coating. MALDI-MSI was performed to acquire spatially resolved molecular signals across tissue sections, generating ion heat maps for distinct protein distributions. **(B)** Parallel FFPE tissue sections were digested, and peptides were extracted for LC-MS/MS analysis using high-resolution Orbitrap mass spectrometry. Identified peptides were label-free quantified to determine fold change enrichments. This workflow enabled the identification and spatial mapping of thymic protein biomarkers, facilitating insights into thymic compartmentalization and regeneration.

Figure 2. Mouse Model of Cyclophosphamide-Induced Thymic Involution. (A-E) The key histological features and compartments of the murine thymus, using Hematoxylin & Eosin (H&E) staining. **(A)** Whole murine thymus, segmented into lobes, lobules through connective tissue capsule and septa, and compartmentalized into outer cortex and inner medulla. **(B)** Magnified insert of the black dotted box in A, revealing a thymic lobule. **(C-D)** Magnified inserts of the black dotted boxes in B, revealing cellular components of the thymic capsule **(C)** or the interlobular septa **(D)**. **(E)** Magnified insert of the white-dotted box in B, revealing cellular components of the corticomedullary junction. **(F)** Pipeline of the mouse model of cyclophosphamide-induced thymic involution. The regenerative process is monitored on a weekly basis following the last dose of chemotherapy (day 0) for up to five weeks (day 35). MALDI-MSI coupled to LC-MS/MS was conducted on day 21, i.e., three weeks following the last dose of chemotherapy. **(G)** Representative H&E sections of whole murine thymi at the distinct timepoints of thymic regeneration after cyclophosphamide insult, as indicated in F. The rebound hyperplasia is notable on days 21 and 28. **(H)** Investigation of thymic lobules during rebound hyperplasia, reveals the maintenance of the overall lobular architecture, albeit with a vast thickening of the lobules, and the disturbed corticomedullary ratio, mostly attributable to increased proliferation of thymocytes in the cortical zone. *CMJ, corticomedullary junction; Veh, vehicle; Ctx, cyclophosphamide.*

Figure 3. Assessing Protein Distribution in Thymic Compartments. (A) Transverse sections of murine thymi from animals receiving either cyclophosphamide (Ctx) or vehicle (Ctrl and then sacrificed three weeks following termination of treatments, and stained with H&E. Dotted black lines indicate various thymic compartments, such as perithymic stroma (s), cortex (c), and medulla (m), identified by their unique histological features. **(B-D)** Molecular images constructed from selected masses show a specific signal at 1454 Da **(B)**, 946 Da **(C)**, and 1337 Da **(D)**. These protein ions signals demonstrate unique and diverse compartmentalization within the thymic structures, with *m/z* 1454 preferentially localized to the thymic capsule and the perithymic stromal tissues **(B)**, while *m/z* 946 **(C)** and *m/z* 1337 **(D)** mostly found in the thymic parenchyma with stronger localization to the medullary or cortical compartments, respectively. However, disturbances in the compartmentalization of the *m/z* 946 and *m/z* 1454 signals is catured in the Ctx-treated thymi, suggesting spatiotemporal changes of the corresponding protein ions. Dotted black boxes in B through D indicate the medullary compartments, as co-registered from the accompanying H&E in A.

Figure 4. Proteomic analysis of thymic peptides from cyclophosphamide-treated and control mice. (A) Total number of peptides and proteins identified by LC-MS/MS from thymic tissue sections of cyclophosphamide-treated and vehicle-treated mice. **(B)** Log2-transformed fold changes of protein abundances between treated and control samples, highlighting differentially expressed proteins. **(C)** Distribution of protein abundances showing a small subset of highly abundant proteins and the majority exhibiting lower abundances. These findings provide a comprehensive proteomic profile of the thymus, identifying candidate markers for thymic compartmentalization and regeneration following chemotherapy.

Figure 5. PepBridge scoring system for MALDI-LC-MS/MS peak matching and identification of peptide candidates. (A) Workflow illustrating the PepBridge pipeline for matching MALDI-MSI peaks with LC-MS/MS peptide identifications. A mass filter of ±1 Da was applied to account for the lower resolution of MALDI-TOF, yielding ~23,000 matches, which were further filtered using a signal-to-noise ratio cutoff of 2.0. **(B)** Final filtered dataset showing 676 peptide matches after applying the scoring criteria. **(C-E)** Scoring metrics used in the PepBridge pipeline: **(C)** delta fold change between MALDI and LC-MS/MS, **(D)** delta mass difference, and **(E)** MALDI intensity. Peptides were ranked based on the combined scores from these metrics. The pipeline enabled confident identification of peptide candidates, narrowing the list to 68 high-confidence peptides associated with thymic compartmentalization and regeneration.

Figure 6. Protein-protein interaction (PPI) analysis of 68 candidate proteins, identified through PepBridge in vehicle- and chemotherapy-treated murine thymi. The network was constructed using STRING v12.0[38]. Proteins were organized into distinct color-coded clusters using an in-built feature for k-means clustering. Associations between proteins are visualized using the medium confidence (0.4) modality.

Figure 7. Correlation between MALDI-MSI and KRT5/8 Immunofluorescence. (A-B) KRT8 signal constructed from MALDI-MSI molecular images (left) along with their paired KRT5 and -8 immunofluorescence (right) on the sequential thymic sections of a cyclophosphamide-treated mouse (A), or a vehicle-treated mouse (B). Co-registration reveals mild shifts in the morphology and topography of the tissue, although most compartments can be captured. The yellow-dotted segments shown in the Ctrl animal on the right have been detached during the preparation and the processing of the MALDI-MSI and LC-MS/MS pipelines, and as such do not correspond to any segment on the MALDI-MSI acquisition. Impressively, the remaining component can be co-registered perfectly with the MALDI-MSI acquisition. Small-dotted boxes corresponding to the letters C, D, E, F, G and H, demonstrate the same fields-of-view in the MALDI-MSI acquisitions and the corresponding multiplex-IF sequential slides. **(C-H)** Magnified inserts of the six fields-of-view indicated in the dotted boxes in A and B, assessed by multiplexed immunofluorescence, for DAPI (nuclear stain), Keratin-5 (KRT5) and Keratin-8 (KRT8). C, E, and G correspond to the three fields-of-view in the cyclophosphamide (Ctx)-treated animal. D, F, and H correspond to the three fields-of-view in the vehicle (Ctrl)-treated animal. Hyphenated versions of these images, i.e., C', D', E', F', G', and H' represent magnified inserts of the white-dotted boxes in each corresponding figure, revealing in high-resolution and single-channels (top, KRT5; bottom, KRT8) the cellular details from their parental images. White-dotted lines correspond to the corticomedullary boundaries, as confirmed by KRT5 signal distribution and intensity, with the medulla staining as $KRT5^{high}$ while other compartments as $KRT5^{-}$ or $KRT5^{low}$.

Figure 8. Immunolocalization of Novel Biomarkers of Thymic Compartmentalization in Murine Thymi at Cyclophosphamide-Induced Rebound Hyperplasia. Validation of three novel markers identified through our new MALDI-MSI pipeline, nucleoportin Tpr (TPR) **(A-D)**, cysteine and glycine-rich protein-3 (CSRP3) **(E-H)**, tubulin-specific chaperone-A (TBCA) **(I-L)**. For each immunolabelled protein a series of sequential representations is reported in a similar manner. The top rows represent cyclophosphamide (Ctx)-treated mice, while the bottom rows (hyphenated versions) represent vehicle (Ctrl)-treated mice. The first column reveals the molecular image of the respective protein, as obtained by MALDI-MSI acquisition, in this case, TPR (A-A'), CSRP3 (E-E'), and TBCA (I-I'). The second column reveals the immunolocalization of each respective protein and condition, using multiplex-immunofluorescence in paraffin-embedded tissues, and fields-of-view are representative of at least N=3, in this case, TPR (B-B'), CSRP3 (F-F'), and TBCA (J-J'). In all cases, DAPI was used as nuclear stain, to document the presence of tissue, and demarcate the corticomedullary junction (white-dotted lines). C, Cortex; M, Medulla; white-dotted lines indicate corticomedullary junctions. In each image a white

line (206 pixels for B, B’, F, F’ and 137 pixels for J, J’) crosses through the corticomedullary junctions and is used for line profiling in the next column. In the third column, the normalized signal intensity of the corresponding protein is plotted along the line profile, in this case, TPR (C-C’), CSRP3 (G-G’), and TBCA (K-K’). The black dotted lines indicate the pixel which segments the line into its cortical (left) and medullary (right) side. Intensity values are normalized to the maximum intensity observed from the two line-profiles of the same immunolabelled protein. The line profiles are representations of at least N=20 lines measured in each condition. The fourth and fifth columns represent higher magnification of the region around the line profiles of the second column. They reveal at cellular detail the precise immunolocalization of each respective protein and condition, using multiplex-immunofluorescence in paraffin-embedded tissues, and fields-of-view are representative of at least N=10, in this case, TPR (D-D’), CSRP3 (H-H’), and TBCA (L-L’). For each example, the fourth column (left) is a merged image including DAPI as a nuclear stain, while the fifth column (right) is a single-channel of the corresponding immunolabelled protein. White-dotted lines indicate the corticomedullary junction.

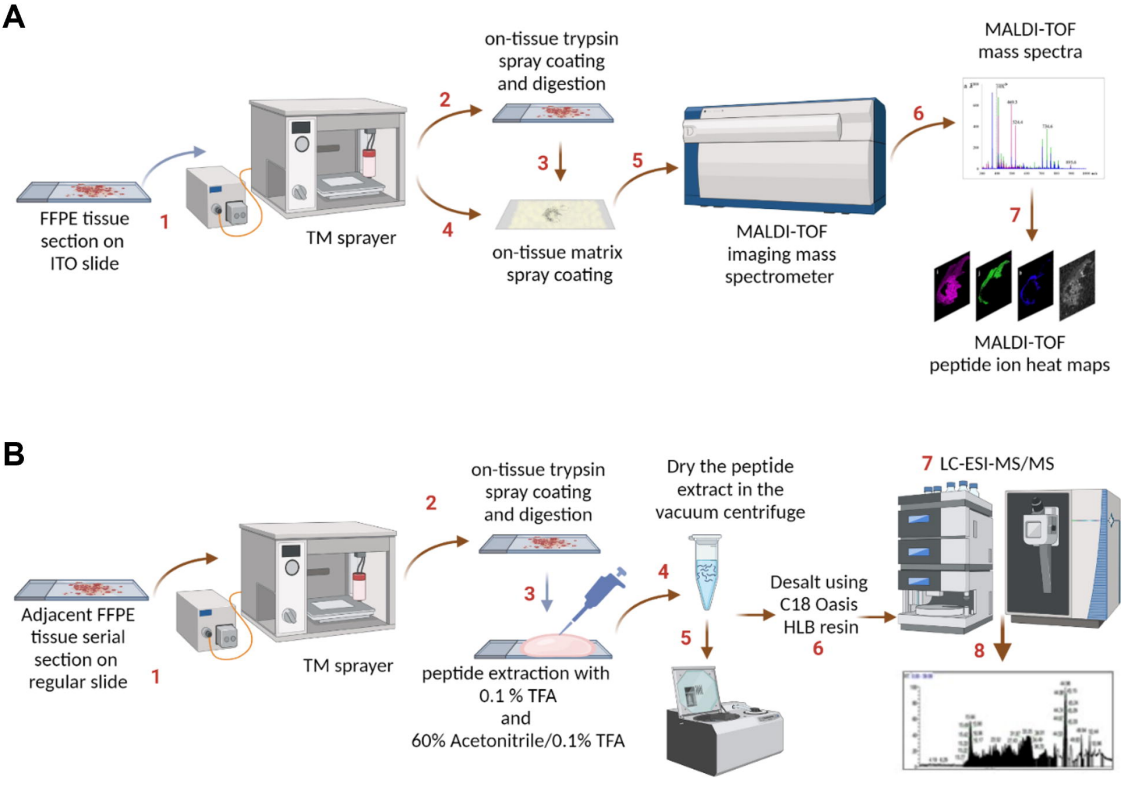
A
FFPE tissue section on ITO slide
1
TM sprayer
2
on-tissue trypsin spray coating and digestion
3
4
on-tissue matrix spray coating
5
MALDI-TOF imaging mass spectrometer
6
MALDI-TOF mass spectra
7
MALDI-TOF peptide ion heat maps
B
Adjacent FFPE tissue serial section on regular slide
1
TM sprayer
2
on-tissue trypsin spray coating and digestion
3
peptide extraction with 0.1 % TFA and 60% Acetonitrile/0.1% TFA
4
Dry the peptide extract in the vacuum centrifuge
5
Desalt using C18 Oasis HLB resin
6
7 LC-ESI-MS/MS
8

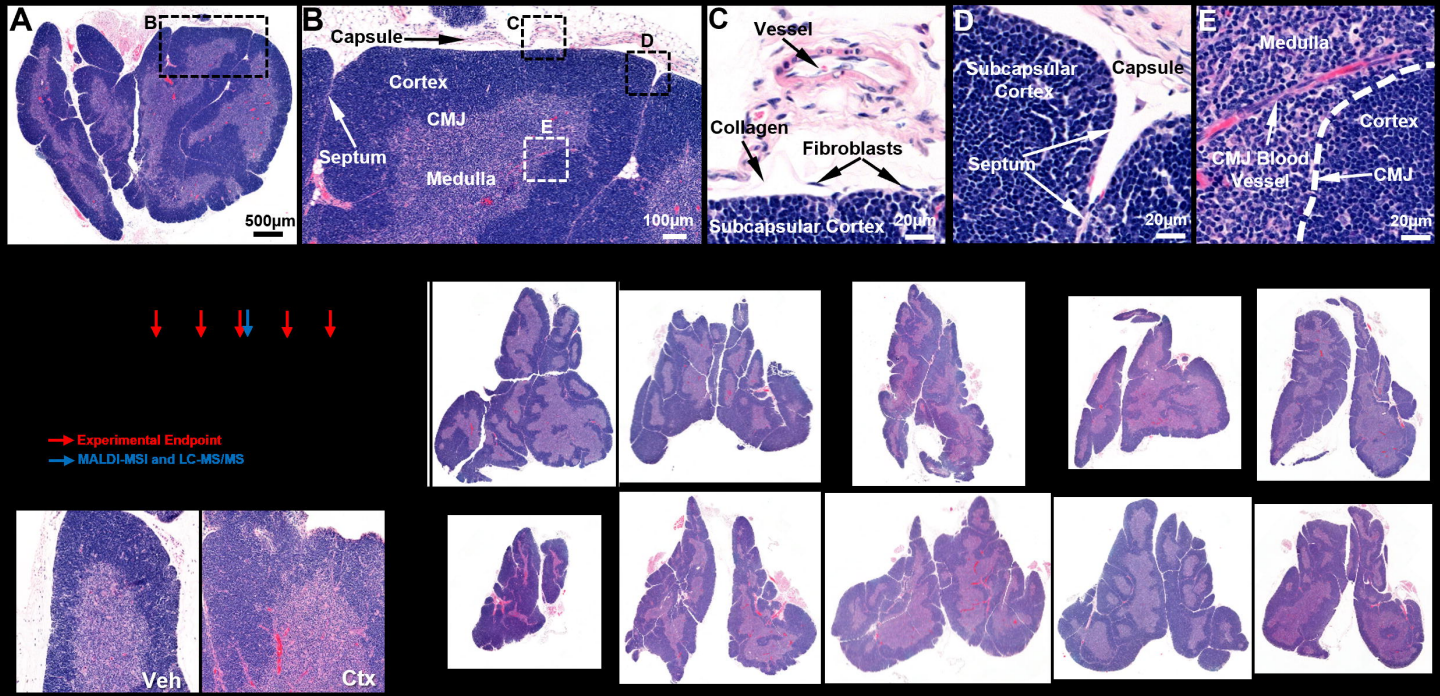
A
B
500µm
B
Capsule
C
D
Cortex
CMJ
E
Septum
Medulla
100µm
C
Vessel
Collagen
Fibroblasts
Subcapsular Cortex
20µm
D
Subcapsular Cortex
Capsule
Septum
20µm
E
Medulla
Cortex
CMJ Blood Vessel
CMJ
20µm
Experimental Endpoint
MALDI-MSI and LC-MS/MS
Veh
Ctx

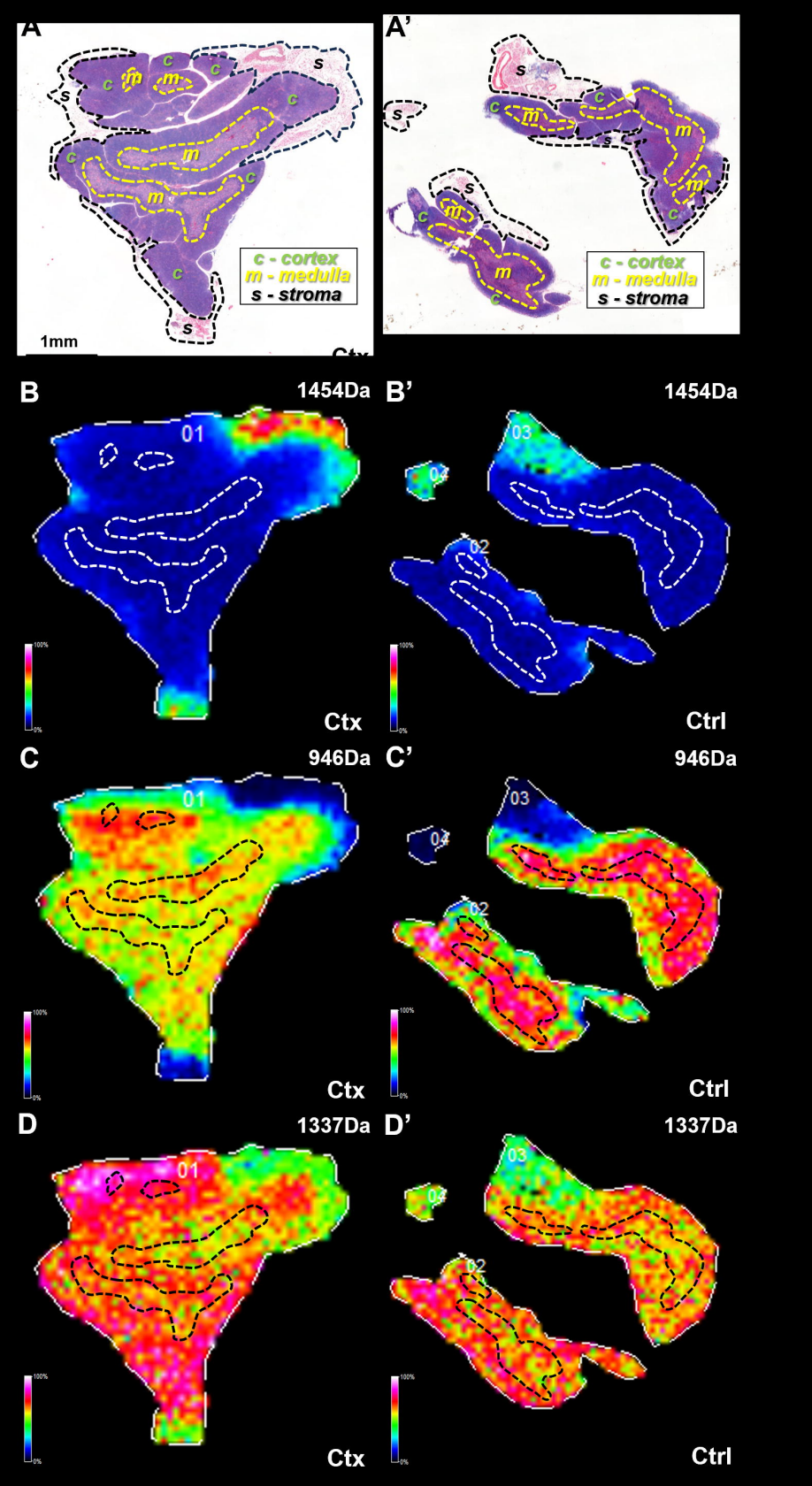
A
c - cortex
m - medulla
s - stroma
1mm
A'
c - cortex
m - medulla
s - stroma
B
1454Da
01
Ctx
B'
1454Da
03
04
02
Ctrl
C
946Da
01
Ctx
C'
946Da
03
04
02
Ctrl
D
1337Da
01
Ctx
D'
1337Da
03
04
02
Ctrl

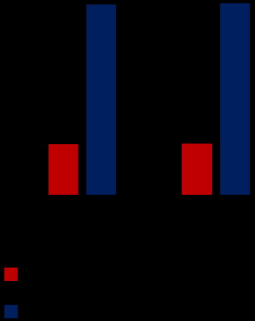

NFGPTGIGFGGLTQQVEK_Csrp
3
VATVSLPR_Tryp
LEAAYTDLQQILESEK_Tbca
TDGFAEAIHSPQVAGVPR_Tpr
80
LIYDFIEDQGGLEAVR_Was
AEAETMYQIK_Krt8
SLYNVGGSK_Krt5

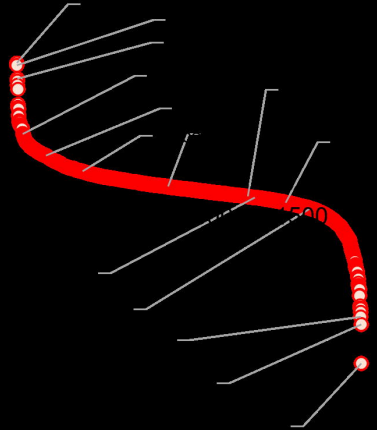
500

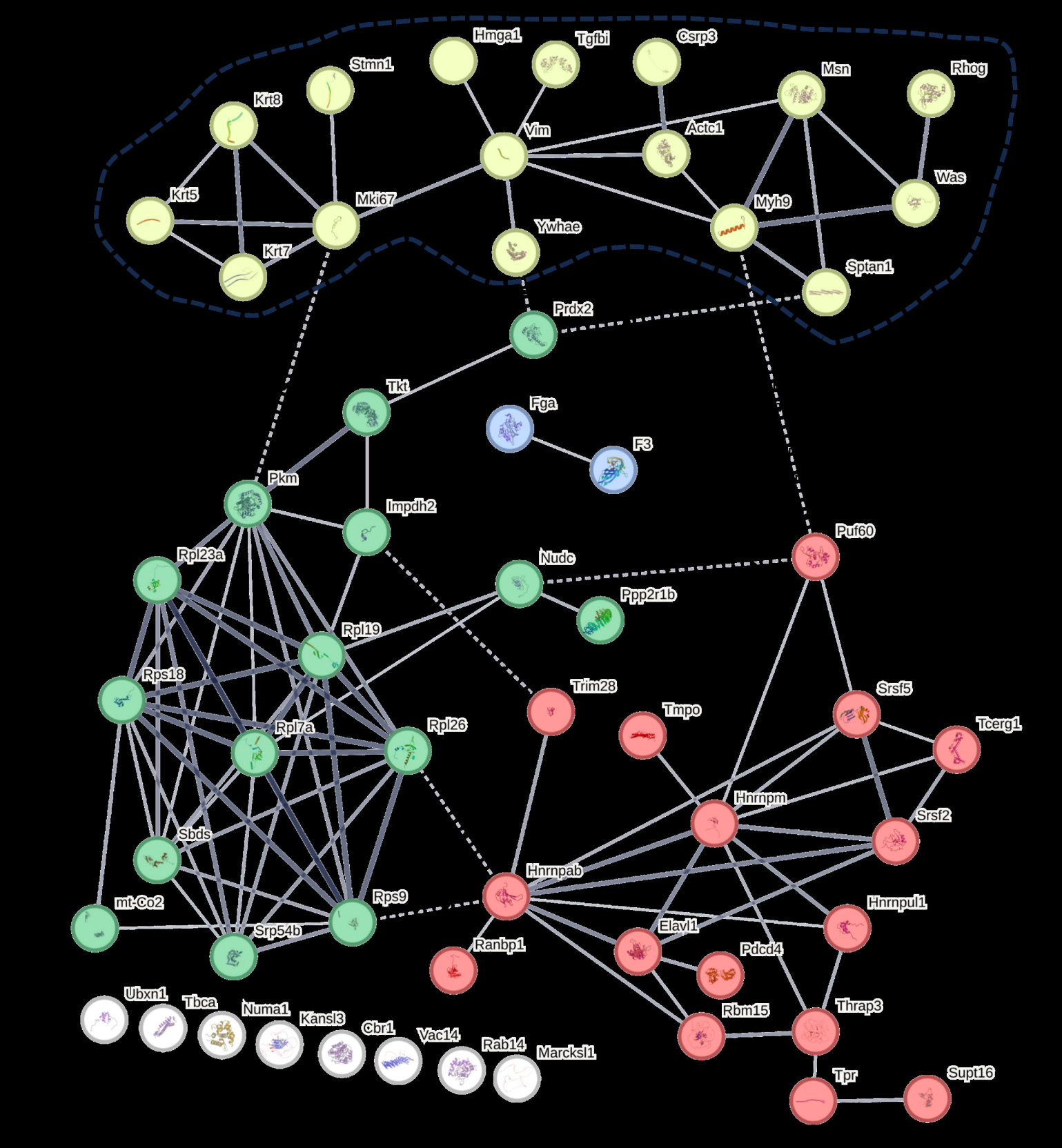
Hmga1
Tgfbi
Csrp3
Stmn1
Msn
Rhog
Krt8
Vim
Actc1
Was
Krt5
Mki67
Myh9
Ywhae
Krt7
Sptan1
Prdx2
Tkt
Fga
F3
Pkm
Impdh2
Puf60
Rpl23a
Nudc
Ppp2r1b
Rpl19
Rps18
Trim28
Srsf5
Tmpo
Tcerg1
Rpl7a
Rpl26
Hnrnpm
Srsf2
Sbds
Hnrnpab
Rps9
mt-Co2
Hnrnpul1
Srp54b
Elavl1
Ranbp1
Pdcd4
Ubxn1
Tbca
Numa1
Kansl3
Cbr1
Vac14
Rab14
Marcksl1
Rbm15
Thrap3
Tpr
Supt16

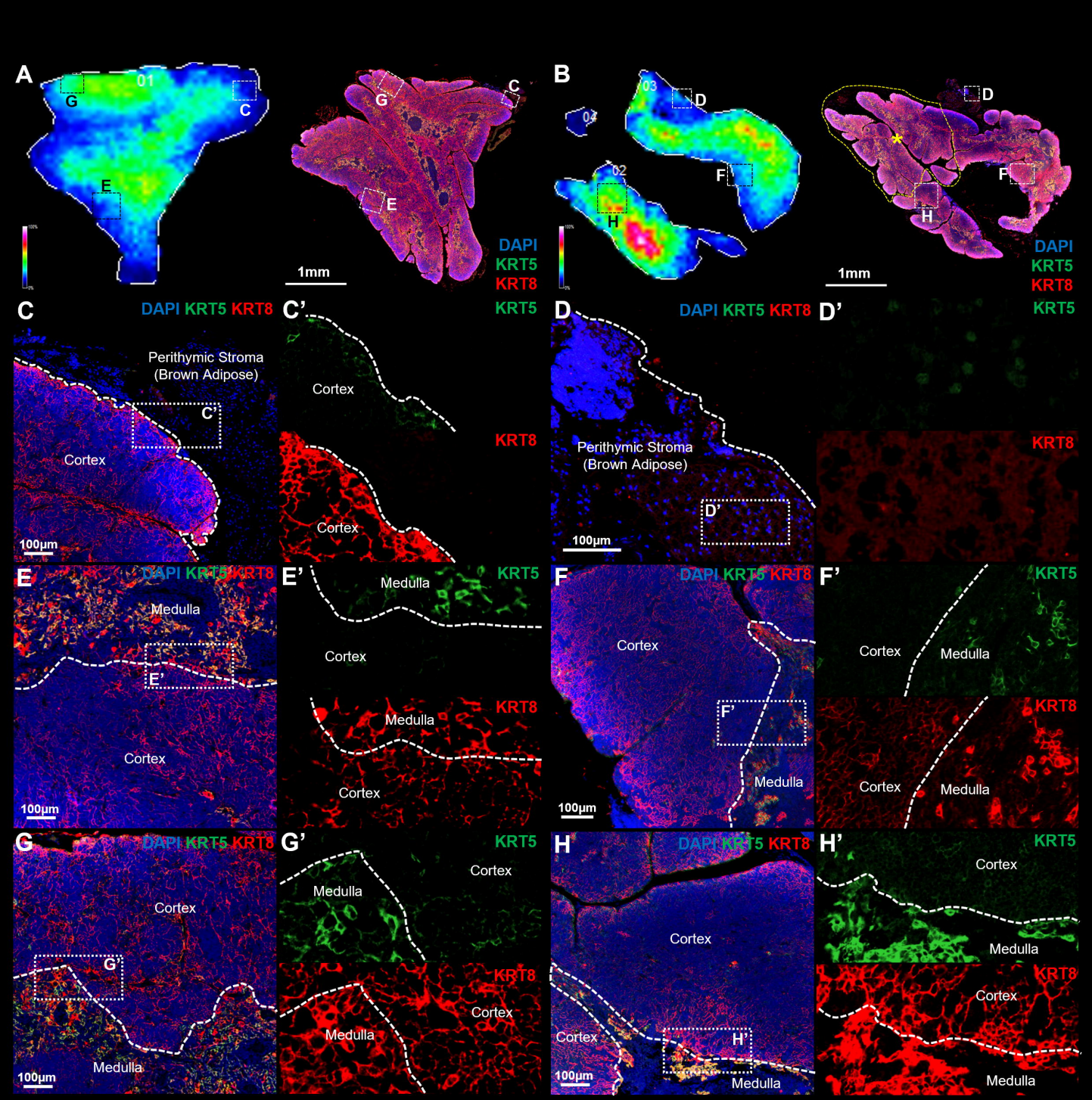
A
01
G
C
E
B
03
D
04
02
F
H
1mm
DAPI
KRT5
KRT8
C
DAPI KRT5 KRT8
Perithymic Stroma
(Brown Adipose)
C'
Cortex
100µm
C'
KRT5
Cortex
KRT8
Cortex
D
DAPI KRT5 KRT8
Perithymic Stroma
(Brown Adipose)
D'
100µm
D'
KRT5
KRT8
E
DAPI KRT5 KRT8
Medulla
E'
Cortex
100µm
E'
KRT5
Medulla
Cortex
KRT8
Medulla
Cortex
F
DAPI KRT5 KRT8
Cortex
F'
Medulla
100µm
F'
KRT5
Cortex
Medulla
KRT8
Cortex
Medulla
G
DAPI KRT5 KRT8
Cortex
G'
Medulla
100µm
G'
KRT5
Cortex
Medulla
KRT8
Cortex
Medulla
H
DAPI KRT5 KRT8
Cortex
Cortex
H'
Medulla
100µm
H'
KRT5
Cortex
Medulla
KRT8
Cortex
Medulla

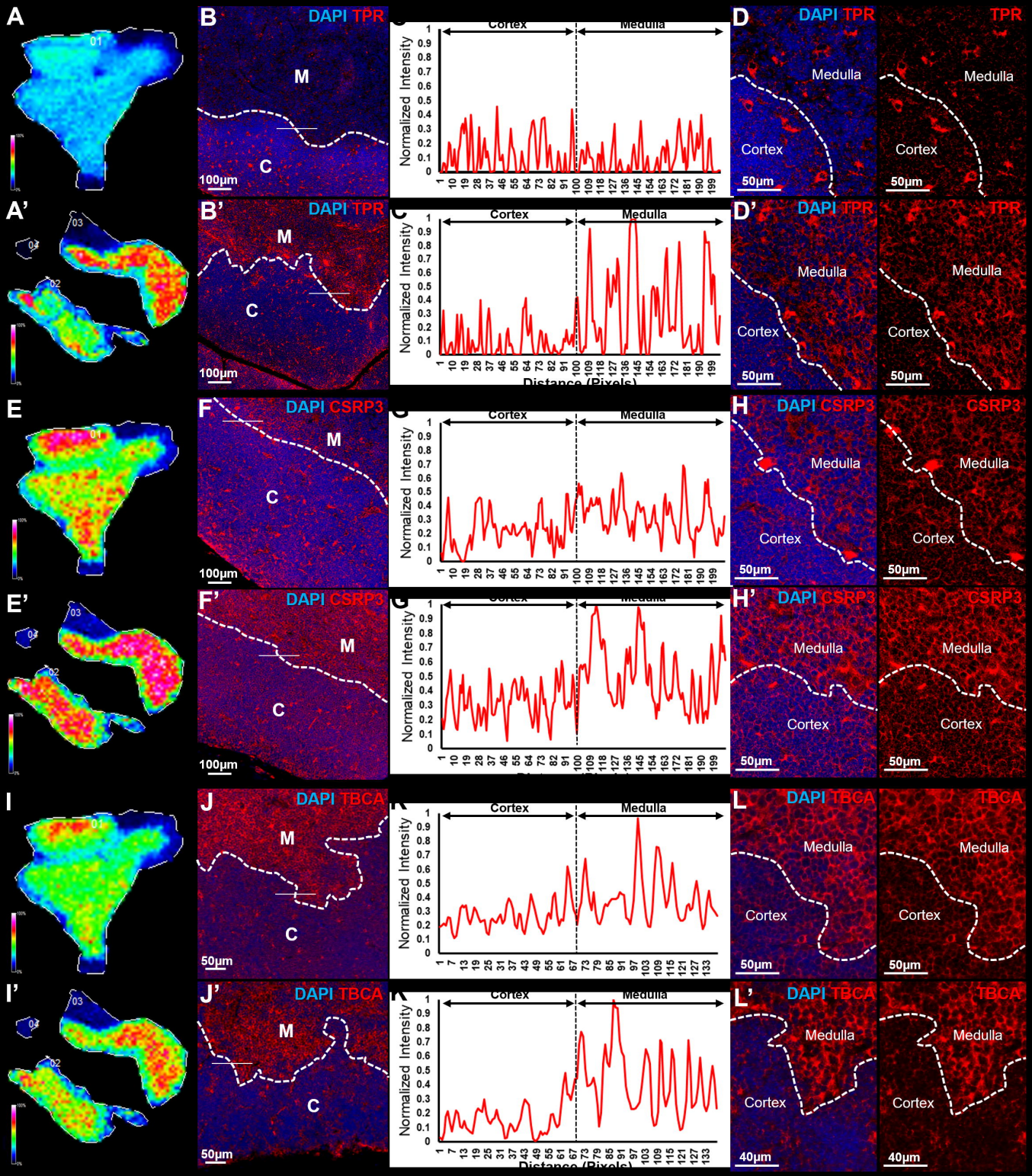
A
B
DAPI TPR
M
C
100µm
C
Cortex
Medulla
Normalized Intensity
D
DAPI TPR
TPR
Medulla
Cortex
50µm
A'
B'
DAPI TPR
C'
Distance (Pixels)
D'
E
F
DAPI CSRP3
G
H
DAPI CSRP3
CSRP3
E'
F'
G'
H'
I
J
DAPI TBCA
K
L
DAPI TBCA
TBCA
40µm
I'
J'
K'
L'